Synthesis and Structural Properties of ZnO Nano-crystallites and their Application

A Thesis

Submission in Partial Fulfilment of the Requirements for the Award of Degree

Of

MASTER OF TECHNOLOGY

In

NANOSCIENCE AND TECHNOLOGY

Submitted by

Deepak Kumar

(Roll No. 2K19/NST/01)

Under the supervision of

Dr. Mohan Singh Mehata

(ASSISTANT PROFESSOR)

DEPARTMENT OF APPLIED PHYSICS

Delhi Technological University

(Formerly Delhi College of Engineering)

Bawana Road, Delhi -110042

July-2021

I, Deepak Kumar, Roll No. 2K19/NST/01 of M.Tech. Nanoscience and Technology, hereby declare that the Research Project Thesis titled *"Synthesis and Structural Properties of ZnO Nano-crystallites and their Application"*, which is submitted by me to the Department of Applied Physics, Delhi Technological University, Delhi in partial fulfillment of the requirement for the award of the degree of Master of Technology is original and not copied from any source without proper citation. This work has not previously formed the basis for the award of any Degree, Diploma Associateship, Fellowship, or other similar title or recognition.

Place, Delhi, India
Deepak Kumar

Date: 03/08/2021

2

CERTIFICATE

I hereby certify that the Research Project Thesis titled *"Synthesis and Structural Properties of ZnO Nano-crystallites and their Application"* by Deepak Kumar, Roll No. 2K19/NST/01, Department of Applied Physics, Delhi, in partial fulfillment of the requirement for the award of the degree of Master of Technology, is a record of the project work carried out by the student under my supervision. To the best of my knowledge, this work has not been submitted in part or full for any Degree or Diploma to this University or elsewhere.

3.8.2021

Place: Delhi

Date: 25.07.2021

Dr. M. S. Mehata

Supervisor

ACKNOWLEDGEMENT

Table of Contents

List of Figures

Abstract

The diamagnetic zinc oxide (ZnO) nano-crystallites were synthesized via the sol-gel method. The X-ray diffraction (XRD), field emission scanning electron microscope (FESEM) were used for structural characterization. The XRD pattern demonstrates that the ZnO nanoparticles (NPs) have a wurtzite structure with an average crystallite size of ~20 nm. The FESEM and EDAX (energy- dispersive x-ray analysis) confirm the particles are in granular, spherical, and rod-like mixed-phase. The absorption spectra show a redshift and observed bandgap (Bg) energy of about 3.17 eV, which might attribute because of the oxygen vacancies. Further, photoluminescence (PL) exhibits dual peaks at wavelengths 430 and 550 nm, which may be assigned due to defects induced at the surface of the NPs. The vibrating sample magnetometer (VSM) study demonstrates the diamagnetic behavior of zinc oxide nanoparticles at 300 K. The photocatalytic effectiveness of the ZnO NPs was examined under UV irradiation by decomposing a Congo red (CR) dye considering as an organic water pollutant. The leading absorption peak of CR dye decreases with the UV irradiation time. The complete decolorization of the CR dye was observed after 150 min with the reaction rate constant of 0.018 min^{-1}.

Chapter 1

1.1 Introduction to Nanotechnology and Nanoscience:

International Union of Pure and Applied Chemistry (IUPAC) has defined the word nanomaterials as materials with the size lesser than 100 nm (1 nm = 10^{-9} m) at least along one dimension. The study of these nanomaterials and their fundamental principles is called "Nanoscience", and applying these materials into functional devices at the nanoscale is known as "*Nanotechnology.*" The uniqueness of nanoscale lies in the fact that at this scale, general properties of material like melting point, hardness and conductivity change. We can say that at the nanoscale, the fundamental properties of a material depend only on its size. Because of these exciting nanoscale materials, physicists, chemists, electrical, mechanical and computer engineers got attracted to nanotechnology for futuristic nanodevices. The study of such nanomaterials creates great opportunities in materials science, especially in solid-state physics, condensed-matter physics, biology, electrical engineering, and other disciplines, as nanoscience closes the gap between individual atoms and bulk materials. As the size of a material decreases to nano range, applications of the material increase because of the change in its properties. Of importance are semiconductor nanomaterials that exhibit unique optical, electrical, size-dependent electrical, and chemical properties, which are largely due to the quantum size effect and large volume surface-to-volume ratio.

Nanomaterials occur naturally, but engineered nanomaterials are of intense interest as someone can design these as per scientific, industrial and commercial requirements. Many nanomaterials can be found in everyday items like cosmetics, vehicle tires, stain-resistant cloths, sporting goods and electronics. They are also used in the medical field for imaging, diagnosis, and drug delivery purposes. Besides producing nanomaterials for their use, there are

millions of nanoparticles (NPs) that every person has been exposed to; we inhale them with each respire and devour them with every drink.

Some questions arise to mind also that what was the foundation of nanotechnology? So that, we explain the history of nanotechnology. History of Nanotechnology? [1].

1959. The idea of "Nanotechnology" was first recognized in a talk by *Richard Feynman* at the "*American Physical Society*" at Caltech.

1974. *Norio Taniguchi* was a professor at "*Tokyo Science University,*" and he has coined "*Nanotechnology*" in his semiconductor processing, i.e., Thin-film deposition and ion-sputtering machine.

1986. Nanotechnology/Nanoscience has been heightened because the invention of the "*Atomic Force Microscope*" plays a vital role in designing/characterized nanomaterials.

1987. *Massachusetts Institute of Technology* held its first university meeting/ conference on "*Exploring Nanotechnology*".

1988. The *Stanford University* ongoing first academia course, "*Nanotechnology and Exploring Nanotechnology*".

1996. *International Business Communications* held a conference on the *"Biological Approaches and Novel Applications for Molecular Nanotechnology"*.

1997. "*Tissue growth on nanostructures compared with currently used materials*" was the first communicated research.

2000. The *"US National Nanotechnology Initiative"* was implemented in the US by the President of the US (Clinton).

2003. This year worldwide, countries are interested in Nanotechnology/Nanoscience.

Interest in nanotechnology was increased with advanced techniques SEM and Transmission electron microscopy (TEM), which helps to see the nanoworld more clearly and more closely. Then a slow and continuous development in nanotechnology was continued. In 1985, three scientists, Richard E. Smalley, Robert F. Curl, and Harold W. Kroto successfully discovered a novel structure of carbon called buckminsterfullerene (a combination of sixty carbon atoms). For this, they were awarded Nobel Prize in 1996. In 2010, Andre Geim and

Konstantin Novoselov had honor with the noble prize for "ground-breaking experiments regarding the two-dimensional material graphene and illustrate the concept of graphene as a robust atomic-scale scaffold based on which new two-dimensional materials with desired electronic and optical properties can be achieved by attaching different atoms and molecules.

1.2 Advances in Nanomaterials:

Following the antecedent two decades, there have been multitudinous advancements in nanomaterials and their characterization. Michael Faraday introduced the first article about the synthesis of nanomaterials in 1850 and he described the synthesis of colloidal gold NPs in that article. Then not long later, in 1940, fumed and precipitated silica NPs were produced for the first experience that acts as a replacement for carbon black extremely fine in size for the strengthening of rubber. After this stupendous success, the application of the amorphous NPs was spread in daily use of household and other products ranging from non-dairy coffee creamers to automobile tires, catalysts and optical fibers. In the 1960s and 1970s, metal nanoparticles successfully were used to fabricate magnetic tape recording. The Spanish civilization invented an ancient unique luminous pigment, Maya blue using the hybrid nanostructured materials with superlattice amorphous silicates of 1.4 nm. This material displays extraordinary durability and holds many different novel optical and electrical phenomena that are more charming for a inclusive variety of applications and electronics, solar cells, memory storage, and aerospace, including ointment sectors [2]. This material exhibits exceptional strength and possesses many other electrical and optical properties, making it attractive for a wide range of applications, including electronics, solar cells, and memory storage, aerospace and lubricant sectors [3].

1.3 How Nanomaterials Differ from Bulk Counterparts??

When we move from the larger state of a substance to its nanoscale, we see changes in almost all the properties (electrical, structural, and optical) of that material. The force of attraction in

the bulk materials is very strong. These forces are feeble and unsaturated while increasing in their reactivity of the materials at the nanoscale [4].

- *Increased relative surface area or large surface area to volume ratio*
- *Quantum confinement effect*

Surface Influences:

When we move material from the microscale to the nanoscale, we see that the number of atoms on its surface has increased, as we did not see in bulk materials.

Quantum Confinement Effect:

When any single particle is very small in particle size compared to the electron wavelength, we say that a quantum effect has arisen. To understand the quantum confinement effect, if it is broken down into two parts, quantum and confinement, then studying the particles at the atomic level are called a quantum, while confinement within certain limits of energy restricts the motion of kinematically moving electrons, to do so is called imprisonment. Therefore, as the particle size moves to the nanoscale, its dimensions are limited, and it appears as discrete energy, which increases the bandgap. In contrast, the bandgap is inversely proportional to the wavelength. Therefore, whenever the bandgap increases, its wavelength agrees, which is proved by the emission of blue radiation. In the best example, we can take carbon, also known as non-metal in microscale, but as we move to the nanoscale, it is considered the best conductor. Now the question arises that what is the role of size behind this? What is the fundamental physics beyond the change in conduction of a non-metal? The most straightforward and best answer to this question is quantum confinement. The dimension of the semiconductor materials has below or equal to the Bohr radius of the bulk semiconductor then the quantum confinement effect comes into play. This phenomenon makes semiconductor size-dependent [5].

1.4 Classification of NPs:

Nanostructures can be categorized based on various parameters, including origin, dimensions, and structural shape. The flow chart Fig. 1.1 given below represents the classification of NPs on account of different parameters:
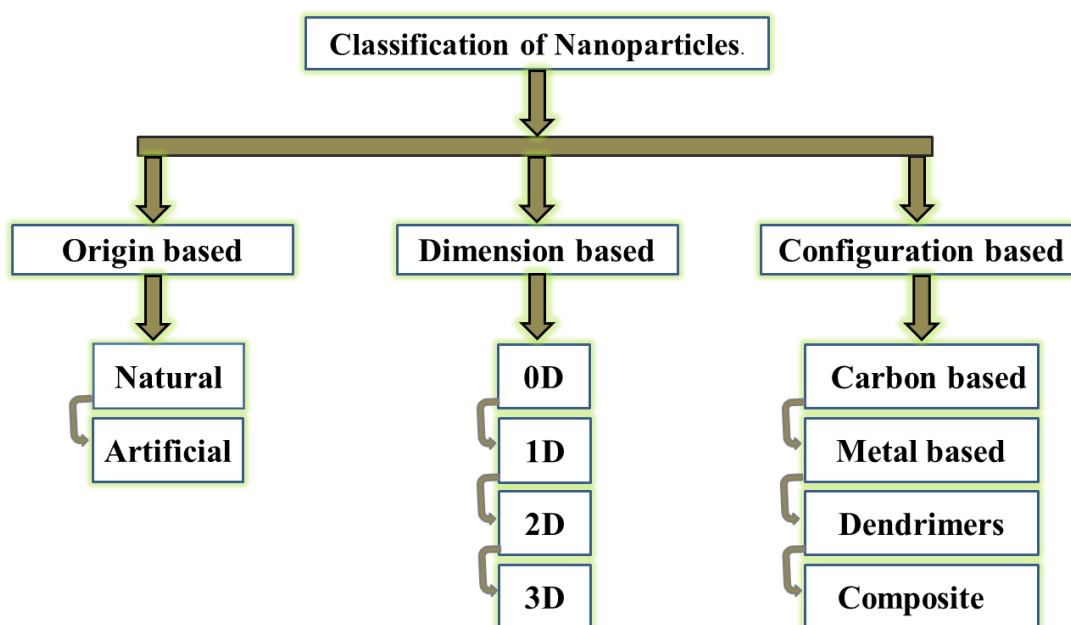
Fig. 1.1: Classification of NPs according to different parameters.

1.5 Origin based NPs:

According to the based on the origin of the NPs are classified into two types:

Natural NPs: This nanoparticle exists in nature and is associated with a natural resource. Some natural nanoparticles include antibodies, amino acids (AAs), viruses, etc. Some examples of realistic NPs are (Ag) proteins (gelatins) in milk are also examples of natural NPs [6].

Artificial NPs: These nanoparticles are synthesized by artificial well-defined synthesis technique. In this technique, numerous classy and unconventional procedures to produce these NPs. Roughly instances of artificial NPs are ZnO nanotubes [7], semiconductors and quantum dots NPs.

1.6 Dimension based NPs:

Basically in these categories of nanoparticles are only defined with their dimensions. It has four dimension-based nanostructures [8].

12

Zero-dimensional (0D): Nanoparticles include three dimensions in this dimension, which come in the nano category, or we can say that the motion of the particle/electron is limited to all three dimensions. These are some instances of the 0D NPs such as silver (Ag), gold (Au), etc. Zero-dimensional (0D) nanomaterials, as well as fullerenes, inorganic quantum dots (QDs), graphene, carbon quantum dots (GQDs), magnetic nanoparticles (MNPs) noble metal nanoparticles, have fascinated spacious research attention in the material sciences [9].

One-dimensional (1D): Only one dimension is allowed to move from the nano range. Rather two dimensions follow the quantum confinement effect, such as nanowires, nanotubes, nanorods like Au, TiO2, ZnO, etc. While these NPs having a width in the nano range and length in micrometer [10].

Two-dimensional (2D): In these dimensions, only one dimension is restricted and the other two are unrestricted to go behind the nanometer range. The restricted dimension one is due to quantum confinement. Thin films, nanowalls, and nanosheets are examples of 2D. The thickness of these NPs is nano range while the area is in the micrometers [11].

Three-dimensional (3D): In these dimension, the motion of a particle is unrestricted in all dimensions. This class can have a dispersion of NPs, bulk powders, bundles of nanowires and nanotubes [11].

1.7 Configuration based NPs:
These nanoparticles are classified based on the structural configurations. It has four types.

Carbon-based nanomaterials: The nature of the nanomaterials in ellipsoids or tubes, hollow spherically. As we know that, fullerenes have kept spherical and Ellipsoid shaped carbon nanomaterials and if cylindrical-shaped called nanotubes [12].

Metal-based nanomaterials: These NPs have metal ions nanomaterials, or the main element is metal, for example, nanosilver, nanogold and some metal oxides like titanium oxide, tin

oxide, and zinc oxide (ZnO). Some semiconductor NPs which are closely packed are also included in this category [13].

Dendrimers: These dimensions in the nano range having vastly branched molecules. There are numerous chains of molecules at the surface of the dendrimer which can be modified to perform specific chemical functions. Poly (amidoamine) or PAMAM dendrimer is the best example[14].

Composites: These range in one, two or three dimensions in a single phase and include nanomaterials multiphase solid materials. Copolymers, colloids and gels are examples of nanocomposites [15].

1.8 Introduction to Zinc Oxide:

The whole world has made itself extremely influential by using semiconductor science. Semiconductor technology is meeting everyone's personal and business needs. Semiconductor technology was first used to developed transistors at Bell Laboratory. It has continued to expand in the semiconductor industry at an incredible pace due to its intense focus. Despite being the first transistor to be manufactured from germanium (Ge), silicon (Si) electronics greatly influenced the global semiconductor industry market due to its relative ease. Integrated circuits, data storage, communications and computing, in particular, are expanding these devices. With excellent physical properties and conventional processing systems, the Si-based semiconductor industry is increasing widely.

ZnO has been investigated as wide bandgap semiconductors for suitability in photocatalytic, magnetic applications. II-VI group of semiconductor ZnO is a multifunctional one with a large exciton binding energy (Eb) 60 meV with a wide bandgap of 3.37 eV. Enabling high temperature and electrical conduction, bring down noise of electronic devices, sustaining

large electric fields, and increasing breakdown voltage are the many benefits of wide bandgap semiconductors[16].

ZnO could produce high efficient UV exciton emission and lasing action at room temperature, which would strongly support short wavelength UV laser applications, it was expected. ZnO has a close focus on its economic value because of its plentiful resources in nature, value-effectiveness, eco-favorable, and easy production method. ZnO displays excellent thermal properties such as high thermal and melting efficiency, conductivity with the thermal expansion coefficient are very lesser, which performs it properly to the ceramic applications [17]. ZnO is not a recently identified applicant in the experimental and manufacturing sectors but has also been invited to research [18].

Though research engagements on ZnO are standing continued for several decades, depending on the specification, niche purposes and innovations are being yielded and strengthened swiftly in a wave coaster form. The primary concerns were triggered by investigating the lattice parameter, synthesis, and characterization of ZnO [19]. Succeeding it was followed by the vibrational properties [18], optical studies [20], and diode properties with metal and semiconductor junctions [21]. Furthermore, numerous articles employed a wide variety of growth procedures, thus paved the way for the advancements in development of great quality, single-crystalline ZnO in bulk, and powder that fired additional interests in ZnO. Room-temperature ultraviolet (UV) laser emissions of ZnO nanoparticles were reported during the late 1990s [22]. The significant obstacle in the improvement of p-type ZnO was written by Look and Claflin [23].

In addition, due to the evolution of nanoscience, unique electrical, mechanical, biochemical, and visible properties were included forward by size decrease due to its surface and quantum confinement effects. Consequently, the vast study of one-dimensional (1D) materials has

grown an advanced edge in nanoscience. Different ZnO nanostructures comprise nanowires, nanorods, nanobelts, tetrapods, nanocubes, nanopyramids, tetrahedrons, nanoribbons, nanowalls, and nanotubes [24] enthusiasm significant interest to develop scientific discoveries. The great crystalline quality and effective carrier properties and its adaptability with the combination of Co to produce ZnO are exceptionally attractive in the field mentioned above of investigation. Hereabouts, some excellent properties such as structural, optical, magnetic, photocatalytic properties, and electrical properties of ZnO will be reviewed, supported by relevant applications.

1.9 Background of Zinc oxide:

ZnO research has a long history, but it developed its recognition as a multipurpose material for photocatalytic, magnetic applications by the last decade. This is because of the improvement in the growth of crystalline ZnO with exceptional optical and structural properties. Monitoring the energy gap is a significant challenge in ZnO research. A small variation in the concentration and expected imperfections can suggestively distress the structural and optical properties.

ZnO is a chemical mixture that become visible as a white powder and is nearly unsolvable in H_2O. According to physics, the group II (Zn) and group VI (O) elements of the periodic table are also called II-VI semiconductors. ZnO is widely used in materials (ceramics, lubricants, adhesives, paints, plastics, batteries, ferrites, pigments and sealants) [25]. It is also used in food items as it is believed to be a source of the Zn nutrient. In the form of zincite, ZnO is present in the earth's crust and is produced synthetically for commercial and industrial purposes. The large bandgap, high electron mobility and good transparency are among its unique properties. ZnO opens the door to look at the production of NPs and their use in scientific and industrial technology because these properties of ZnO combine with simple and inexpensive techniques for researchers. Hexagonal wurtzite, the cubic zinc blende occurs in two crystalline forms of ZnO. Wurtzite ZnO is the largest commonly found crystalline phase of ZnO. Analytically,

wurtzite has lattice parameters determined for ZnO and is a straight bandgap semiconductor with a bandgap value [26].

Thus, bottomless understanding of intrinsic point imperfections and adding impurities are the key factors controlling conductivity. Researchers are trying to control the defect states and associated charge carriers by amending the preparation circumstances and post-growth behaviours like calcination and hydrothermal treatment. Taking into account the photo-induced charge separation ability of ZnO and excellent conductivity of Co, ZnO/Co hybrids are one of the remarkable candidates for optoelectronic applications[27].

1.10 Properties of ZnO:

The tetrahedral coordination in ZnO leads to a non-centrosymmetric structure, one of the most important characteristics which make ZnO a potential candidate for piezoelectric and pyroelectric application [28]. The physical properties of ZnO NPs like molar mass (81.408 g/mol), density (5.606 g/cm^3), melting point (1975°C), boiling point (2360°C), refractive index (2.0041), and solubility in water (0.16 mg/100 mL (30°C), etc. Intrinsic ZnO exhibits n-type material characteristics due to natural defects such as oxygen vacancy (Vo) and zinc interstitials (Zni) [29].

Structural Properties of ZnO:

ZnO crystallizes having two different forms, the hexagonal wurtzite and cubic zinc blende, among which cubic structure is rarely observed. The wurtzite structure is the furthermost frequently obtained and it has the uppermost working stability among other forms. The hexagonal lattice (space group P63mc), and Each Zn^{2+} ion is tetrahedrally surrounded by four O^{2-} ions, and vice versa.
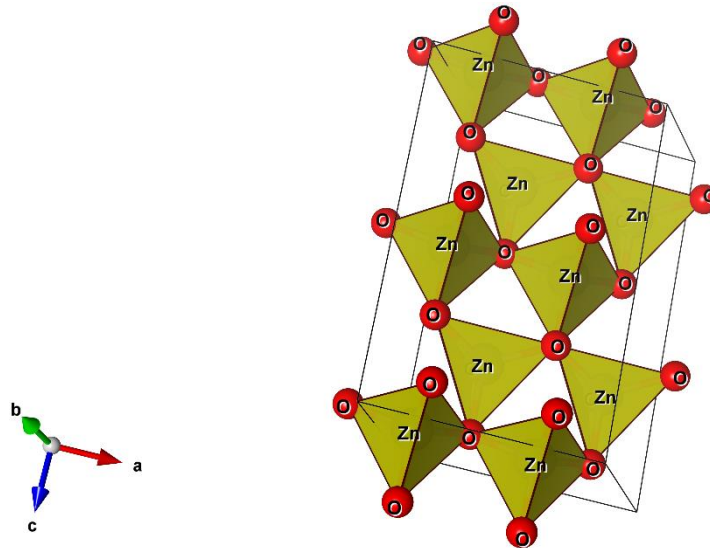
Fig. 1.2: Schematic diagram of the hexagonal wurtzite crystal structure of ZnO.

The tetrahedral coordination means sp^3 hybridized covalent bonding. Nevertheless, these materials have partial ionic character due to the polarity difference. Under room temperature (RT), the wurtzite symmetry thermodynamically stable phase. ZnO having wurtzite structure can be designated as the number of discontinuous planes composed of tetrahedrally coordinated Zn^{2+} and O^{2-} ions set interchangeably along the c-axis as shown in Fig 1.2**.** This tetrahedral coordination results in the lack of inversion symmetry perpendicular to the c-axis. The lattice parameters of the hexagonal unit cell (a = b ≠ c) are a = 3.2495 Å and c = 5.2069 Å respectively[30]. While the atomic fraction (c/a= 1.6329) and many parameters are also calculated like d-spacing values, unit cell volume, and bond length, etc.

Wurtzite ZnO with crystal symmetry C6v and space group P63mc belongs to the hexagonal crystal structure. Figure 1.2 describes an elemental crystal structure of ZnO [31]. This crystal holds the three most typical facets (101), (211), and (001). The first two facets are non-polar and the last is a polar facet. To investigate these surfaces, several techniques are available, like scanning tunnelling microscopy (STM), X-ray diffraction (XRD), low energy electron diffraction (LEED), and scanning tunnelling spectroscopy (STS) [32]. ZnO can accomplish

various morphologies. It can be developed in zero-dimensional (nanoclusters), one-dimensional (nanowires), and two-dimensional (nanotubes) morphologies. Plenty of research has been implemented to learn the mechanism implicated in the growth of ZnO analytically and theoretically [33]. Compared to simple 3-D structures and 2-D nanosheets of ZnO, 1-D crystalline facets make ZnO an unusual and innovative material due to its single-crystalline surface with high surface area.

Optical Properties of ZnO:

The ZnO produces an active emission at room temperature [34]. To be suitable for semiconductors, notably for photocatalytic and magnetic applications. Tunability in the bandgap is an essential condition for design advancement, which can be efficiently performed in ZnO. Particularly ZnO in its powder form, the optical properties can be optimized to more than 80% by adjusting the method parameters of the elected segments [35].

Chemical and Mechanical Properties of ZnO:

Pure ZnO is white in appearance, but when we heat it to a temperature above 300 °C, its colour changes due to thermochromic properties. ZnO absorbs carbon dioxide forming zinc carbonate when exposed to air, whereas it does not dissolve in water and dissolves with acids. It forms zinc sulphate; when it reacts with sulfuric acid, it forms zinc sulphate, while zincate forms, reacting with alkali metals. ZnO is a subtle material with the inflexibility of ~5 GPa at a malleable penetration deepness of 300 nm on the c-axis orientation. ZnO exhibits high heat capacity, thermal conductivity, low thermal expansion and high melting point. Photocatalytic is an important mechanical property of ZnO and among tetrahedrally bonded semiconductors, with the ZnO having the uppermost piezoelectric tensor [36,37]

Magnetic properties:

Magnetic property is one of the attractive properties of semiconductor nanostructures with a spacious area of applications such as magnetic memory media and ferrofluids. Only in the data

storage equipment, generally, magnetic materials are used. Whereas in recent years, it has been observed that magnetic materials perform many functions. In recent years, researchers are exploring the use of spin properties along with electric charges to create a new generation of spintronic devices that are smaller in size and are smarter than traditional silicon devices [38].

Atoms grow in comparison to the bulk of the surface of nanostructured materials. And these surface atoms are in the separate coupling, unlike bulk atoms. The diamagnetic behavior shows that of ZnO in bulk form. Although, numerous researchers have examined room temperature ferromagnetism in bare ZnO nanostructures. The surface-related phenomenon by the Ferromagnetic coupling in ZnO nanostructures. Sundarson et al. [39] summarized that ferromagnetism is a terrestrial characteristic of non-magnetic oxide NPs. Gao et al. [40]analyzed that at the ambient temperature and pressure ferromagnetism in pure ZnO NPs.

On the other hand, seldom do the ferromagnetic nanostructures display unpredictability and begin displaying paramagnetism under remarkable specific size. The ferromagnetic nanostructure can turn to magnetism that does not present hysteresis and magnetization effects not saturate, which is called super-paramagnetism. The ferromagnetism in large-sized nanostructure is due to repetitious regions, which transform to super-paramagnetism with size reduction. In conclusion, the magnetic coercivity vanishes. Mhlongo et al.[41] Reported on the investigation of paramagnetic behaviour in ZnO nanostructures.

1.11 Introduction to dilute magnetic semiconductors:

Current electronic machines operate on the base of charge carriers such as electrons and holes. The single spin of an electron has not been appropriated in current electronic devices. Most prominent modern electronic appliances can prepare signals at a large pace and with authenticity. The principal idea of spintronics is to utilize both the charge and spin of electrons simultaneously to process and store the information. The unrestricted investigation has been

moved to examine numerous dilute magnetic semiconductor (DMS) materials among the relationship towards the advancement of spintronics devices. The replacement of magnetic ions of magnetic elements regularly transitions elements (TE) such as Mn, Co, Cu, Ni, and Fe by substituting some portions of cations of nonmagnetic semiconductors are represented as DMS. The exchange interaction within the spins of the dopant atoms via the carriers in the semiconductor communion issues in the polarization of spin of the transmitters [42,43]. Ferromagnetism collected in the elements as mentioned above is contemplated to be arbitrated by charge carriers. The continuous research for the materials with ferromagnetism with more leading Tc led to examining the oxide-based dilute metal semiconductors. The great electron dopant ability and huge sufficient electron mass of oxide semiconductors are perceived to be pretty effective in achieving great Tc ferromagnetism that addresses them key substances for spintronic devices[44].

Transition element (TE) doped ZnO nanostructures:

Co^{2+}, Mn^{2+}, Cu^{2+}, Ni^{2+}, and Fe^{2+} transition constituent ions are popularly applied against ZnO as dopants to achieve oxide DMS. The structural, optical, electronic, photocatalytic, and magnetic characteristics of the host ZnO are transformed due to the influential hybridization of s and p electrons, including 3d electrons of TE ions. Dietl et al. [45] forecast of attainable demonstration of room temperature ferromagnetism due to carrier-mediated replacing interaction linked with the spin-orbit coupling in TE doped ZnO created a lot of excitement. In sequence to advance the absorption in the evident range, the bandgap of ZnO nanostructure can be transformed by the insertion of TE ions in the lattice of ZnO. The adding of TE ions in ZnO produces trap states inside the energy bandgap, resulting in UV-vis illumination absorption spectra enhancement. The PL emission properties of ZnO NPs can be altered, including TE doping, as per the specification of excellent applications in optoelectronics devices. ZnO has authenticated itself as a reliable photocatalyst under UV light irradiation. The TE doping in

ZnO is great to boost the catalysis efficiency of ZnO by absorbing visible light. It is well known that sunlight contains 45% visible light and less than 10% of UV. Utilization of the 45% visible light and UV can be possible by exchanging extrinsic elements like Co and Cu in ZnO [46].

Co-doped ZnO nanoparticles:

After the doping of Co^{2+} in ZnO can enhance their optical, photocatalytic and magnetic properties. Co-doped ZnO shows captivating visible absorption and emission properties pointing towards their potential applications in UV-Visible photocatalysis. The visible light absorption of Co-doped ZnO NPs is heightened due to the d-d transition of electrons of Co^{2+} ions that assists in the improvement of photocatalysis activity. The fluorescence emission of Co-doped ZnO is normally economical corresponded to the un-doped ZnO nanoparticles. The luminescence properties can be altered for acceptable applications by Co doping in ZnO. Jayakumar et al. reported a fascinating investigation of the morphological transformation of ZnO nanorods to spherical nanoparticles after the substitution of Co, including the aid of a simple chemical method [47]. Li et al. [48] described that pure ZnO particles produce the structure like a 3D flower and have an average size of 550 nm. These are converted with the like-cauliflower nanoclusters having an average size of 120 nm subsequent Co doping in ZnO. Srinatha et al. reported on microstructure with optical phenomenon belongings of Co-doped ZnO nanoparticles synthesized via solution combustion technique [49].

The main reason behind the ferromagnetism at room temperature is Oxygen vacancy and zinc interstitial defects states in Co-doped ZnO and undoped ZnO. According to their investigation Park et al. [50] demonstrate that Co-doped ZnO thin films incorporated by sol-gel coating route presentation paramagnetic form for more moderate doping concentration. Yildirim et al. [51] reported on the structural, morphological, optical and visible light photocatalytic activity of Co-doped ZnO nanoparticles synthesized via the sol-gel method. Poongodi et al. [52] reported the enhanced visible-light photocatalytic and antibacterial activities of Co-doped ZnO

nanostructured thin films synthesized by a sol-gel spin coating method. Gu et al. [53] reported on the tunable room-temperature ferromagnetism by changing oxygen vacancy with the help of annealing of Co-doped ZnO nanoparticles synthesized via the sol-gel method. Phan et al. [54] reported on the research of ferromagnetism due to the interchange interactions of Co^{2+} ions through extrinsic defects in Co-doped ZnO with secondary cubic spinel $ZnCo_2O_4$ phase synthesized by conventional solid-state reaction method. Tseng et al. [55] reported on the spatial non-uniform ferromagnetism in Co-doped ZnO NPs deposited by laser molecular beam epitaxy method and it is connected to bound magnetic polarons.

Defects and Effect of Doping on ZnO:

The doping of ZnO with various elements is one of the key requirements for many applications to boost and regulate its magnetic and optical properties [56]. The as-grown ZnO is an n-type material due to the presence of Oxygen deficiency and Zinc interstitials. Its' n-type conductivity can be controlled by doping it with group III elements like Al, Ga, or In [57]. ZnO-based Dilute Magnetic Semiconductors (DMS) doped with transition metals like Co, Mn, etc., have been studied to be appropriate candidates for room temperature ferromagnetism and large magnetization [58].

1.13 Application of ZnO:

ZnO nanoparticles and their nanostructures have novel applications in magnetic, photocatalytic. ZnO is one of the unique materials that exhibit both semiconducting and piezoelectric properties. ZnO NPs and nanostructures (nanorods, nanoflowers, nanoflakes, nanowires, nanobelts, nanocages, nanocombs, and nanosprings) are grown by using well-known sol-gel, Chemical Precipitation, and hydrothermal reactions. ZnO nanostructures have potential use in different areas in line for their distinctive physical and chemical properties [59].

Luminescence:

The large exciton binding energy at RT can ensure with an efficient exciton emission. As a result, ZnO is recognized as a potential photonic material in the UV-Blue region. Room temperature UV lasing in single-crystalline ZnO nanowires has been demonstrated. Generally, Photoluminescence (PL) spectra of ZnO nanostructures measured with Photoluminescence system show a strong UV emission around 386 nm and a week emission in the visible region. The UV emission must contribute to the near band edge emission of the ZnO. The visible emission corresponds to the singly ionized Oxygen vacancy in ZnO and results from the recombination of a photogenerated hole with the defects [60].

Photocatalytic Activity:

Photocatalysis is an interesting water purification process. It can utilize light energy to activate the oxidation and reduction procedures, which are supervise for removing tenacious and poisonous organic compounds from the water. During photocatalytic application, two different reactions occur at the material surface, (a) an oxidation reaction due to the photo-induced positive hole and (b) a reduction reaction due to the photo-induced negative electrons [61]. Numerous metal oxide semiconductors are used in photocatalysis; among them, ZnO is a promising candidate for environmental applications due to its strong oxidation ability and the fact that it has a direct and wide-bandgap in the near-UV region. Exciton emission processes can persist at or even above room temperature due to their large exciton binding energy. In addition to this, ZnO is a non-toxic and environmentally safe material. It is compatible with living organisms, relatively cheaper material, and can be used for large-scale water treatment plants [62].

Gas Sensing:

Different gases that ZnO nanostructures have detected include ammonia, nitrogen oxide, hydrogen and oxygen. ZnO nanostructures have a huge surface area which enables them to be more susceptible to the adsorption or desorption of gas particles on their surface. [63].

Biosensing:

Non-toxicity, bio-compatibility and high electron transfer rates are some of the exciting properties of ZnO nanostructures that make them favorable for detecting biological entities [64].

UV Detection:

ZnO nanostructures have been applied for UV photodetection by various research groups[65].

UV Lasers:

Growth conditions of ZnO nanostructures can be manipulated to eliminate defects-related emissions allowing them to be applied for UV laser applications [25].

Light-Emitting Diodes:

Research groups like *Harnack et al.* [66] have demonstrated that the electrical characteristics of ZnO nanorods show diode-like behavior allowing their potential use in LEDs.

Solar Cells:

The large surface area and high electron transfer rates of ZnO nanostructures make them potential candidates as electrodes in dye-sensitized solar cells (DSSCs) [67].

Fields Emission Devices:

ZnO nanostructures, particularly with sharp tips have shown good field emission characteristics, making them applicable as electron-emitting sources [68].

Field Effect Transistors:

The ZnO nanostructures act as the channel that controls the current flow from the drain to the sources by manipulating the gate voltage [69].

Chapter 2

2. Literature Review:

A literature survey is the complete and inclusive exploration of numerous research activities done by multiple researchers on an elected area and the briefing of their conclusions. In the modern-day, the attention of many operators in science, technology, and engineering has been attracted to nanoparticles' production and properties. Relevant literature similarly associated with the synthesis and characterization of ZnO and transition metal-doped ZnO nanoparticles are examined and exhibited results.

In this chapter, a literature survey has been studies about the various synthesis techniques of Zinc Oxide and its photocatalytic and magnetic applications. The properties (structural, optical, magnetic, etc.) of ZnO and metal ion-doped ZnO NPs have been reviewed.

Eibner (1911) [70] studied the outcome of illuminated ZnO on organic and inorganic coloring materials. He observed that the dye discoloration took place by adding ZnO under light irradiation.

Baur and Neuweiler (1927) [71] reported that ZnO irradiated with UV light produced H_2O_2 from O_2 and H_2O. They proposed that a simultaneous oxidation and reduction process takes place on the ZnO surface.

Oster and Yamamoto (1966) [72] reviewed the photocatalytic activity (PCA) of ZnO. Using ZnO NPs, they reveal that more effective on the indophenol and diphenyl picrylhydrazyl under ultraviolet (UV) irradiation (365 nm mercury lamp including UV filter). In addition, ZnO NPs was also decreasing silver ion under the ultraviolet and red light. In contrast, mercuric ion was degraded under UV irradiation to give mercury in aqueous suspension in the presence and absence of O_2.

Seung and Yun (1997) [73] were used spray pyrolysis to prepared ZnO NPs and characterized NPs by TEM and XRD analyses to confirm particle size (5-12 nm). These synthesized ZnO NPs show much more effective photocatalytic activity to degrade trichloroethylene (TCE) than bulk ZnO and commercial TiO_2 (Degussa P25) under UV-vis irradiation.

Jing et al. (2005) [74] applied chemical precipitation method to synthesized ZnO nanoparticles. They degraded the gas-phase nC7H16 by the photocatalytic process and used ZnO as a catalyst. In this experiment, they have proposed a relation between surface oxygen vacancies and photocatalytic activity and outcome PCA efficiency was increases with surface oxygen vacancy of NPs.

Wang et al. (2008) [75] studied and synthesized ZnO nanoflowers by hydrothermal method and demonstrated that the ZnO structure might be tuned by changing the pH of the solution. The nanoflower of ZnO is made of nanorods and having Dia 100 nm, length 1-1.5 micrometer. As a result, the PCA efficiency can be heightened under UV light and degrade 4- chlorophenol (4-CP) easily compared to ZnO nanorods because oxygen vacancies are more at the surface of ZnO nanoflower. The photogenerated electrons capture and efficiently block the recombination of photogenerated electrons and holes because surface oxygen vacancies act as active centers.

Wang et al. (2012) [76] synthesized ZnO with a high concentration of VOs by annealing of ZnO2 precursors. Raman and Raman and XPS studies validated that the concentration of VOs decreases with raising the annealing temperature from 400 to 800 °C. The defective ZnO with VOs showed efficient 2, 4- dichlorophenol photodegradation activity. Additionally, they noticed that the visible light absorption and the PCA efficiency increase with increasing the concentration of VOs.

Balachandran et al. (2016) [77] produced Ag-Bi_2O_3-ZnO heteroarchitecture using the photo deposition-hydrothermal method. As obtained, heterostructure revealed mixed crystal phases

of α-Bi$_2$O^3 and hexagonal wurtzite of ZnO. The Ag-Bi$_2$O$_3$-ZnO displayed a well-organized mixture of nanoparticles and nanosheets morphology. Ag-Bi$_2$O$_3$-ZnO exposed higher absorption in the UV and visible province than Bi$_2$O$_3$ and ZnO. The Ag-Bi$_2$O$_3$-ZnO photocatalyst showed upgraded photocatalytic performance to decompose evens blue, acid red 1, and acid violet 7 under ordinary daylight compared to Bi$_2$O$_3$, Ag-ZnO, Ag-Bi$_2$O$_3$ and ZnO systems at pH 7. Ag-Bi$_2$O$_3$-ZnO was found to be recyclable and stable up to five runs of photocatalytic degradation.

Anupama Chandra et al. (2017) [78] synthesized Cobalt-doped ZnO nanoparticles by chemical method. The structural analysis confirms NPs are hexagonal wurtzite in nature and as cobalt concentration increases, the formation of nanorods increases. The disorder and surface defects of NPs were verified by Raman analysis as validated the incorporation of Co in ZnO NPs. The increase in the band gap energy of ZnO is due to the Co concentration. Pure ZnO showed diamagnetic and superparamagnetic and ferromagnetic behavior was demonstrated as they doped cobalt in the ZnO NPs at room temperature and 2K.

Anupama R. Prasad et al. (2018) [79] were produced ZnO NPs using the green synthesis method and using lemon juice and ethylene glycol. The NPs particle size is uniform and found to be 49 nm in honed faces with nanogranules nature. Synthesized ZnO nanogranules exhibited excellent photodegradation of Methyl blue (MB, 91.17% in 70 min), Congo red (CR, 90% in 35 min), and Rhodamine B (Rh B, 98% in 50 min) dye under UV-irradiation.

Niraj K. Singh et al. (2019) [80] prepared undoped and doped ZnO NPs in an ethanolic medium by well-known low-cost sol-gel technique; as an outcome, the average crystalline size decreased with the doping concentration. From the structural analysis, they are revealed that undoped and doped NPs in the spherical shape. Optical analysis, bandgap energy increases as the doping content increases; the Kubo theory also verifies this phenomenon. Broadening,

intense emission peaks in the visible region are due to oxygen vacancy defects and are directly proportional to cobalt concentration which is confirmed by Photoluminescence (PL) spectra.

E. Bellingeri et al. (2019) [81] prepared pure and Co-doped ZnO thin films transistors using a pulse laser ablation method. The synthesized thin films were used to examine magnetotransport properties by implementing the model of Khosla and fisher model to estimate spin carrier, polarization and magnetization. Magnetization reduction and free carrier concentration with together spin carrier polarization increases.

Chithra P. R et al. (2020) [82] prepared a pure ZnO and Co-doped ZnO chemical precipitation method. They are also demonstrated that the Co content does not affect the wurtzite structure of ZnO NPs. From the UV- Vis spectra, an increment was noticed in the visible region due to the d-d transition of Co concentrations. The presence of Co content in ZnO NPs without disturbing the wurtzite phase or created secondary impurity phase confirmed by X-ray photoelectron spectroscopy (XPS) measurement. Enhancement in the ferromagnetic nature by bound magnetic polarons (BMPs), which can be enable coupling between incorporation of Co accompanying with oxygen vacancies. The pure ZnO's decomposition of the RhB dye exhibited decent photocatalytic degradation, while the doped ZnO lessens the degradation rate. The doped ZnO enhanced magnetism properties by the defects created at the surface and without disturbing pure ZnO give good degradation of organic dye under the solar irradiation.

In the present work ZnO NPs sized approximately 20 nm were developed using sol-gel method and investigated using different techniques namely absorption and emission spectroscopy, XRD, SEM, EDAX, and VSM. The obtained results are discussed in detailed in Chapter 5 along with their application as catalyst for the degradation of industrial dye.

3. Materials and Methods:

Synthesis Materials and Methods of Nanomaterials:

Researchers in material science are continuously researching to develop novel nanomaterials with low cost, better properties, and better functionality than existing nanomaterials. They have developed several physical and chemical methods to synthesize nanomaterials having improved properties, and the scientists have better control over the morphology and size of these nanomaterials. Two basic approaches are followed to synthesize nanomaterials, and all the techniques for the synthesis of nanomaterials can be classified into these basic approaches. These approaches are called Top-down and Bottom-up approaches, which are schematically illustrated in Figure 3.1.
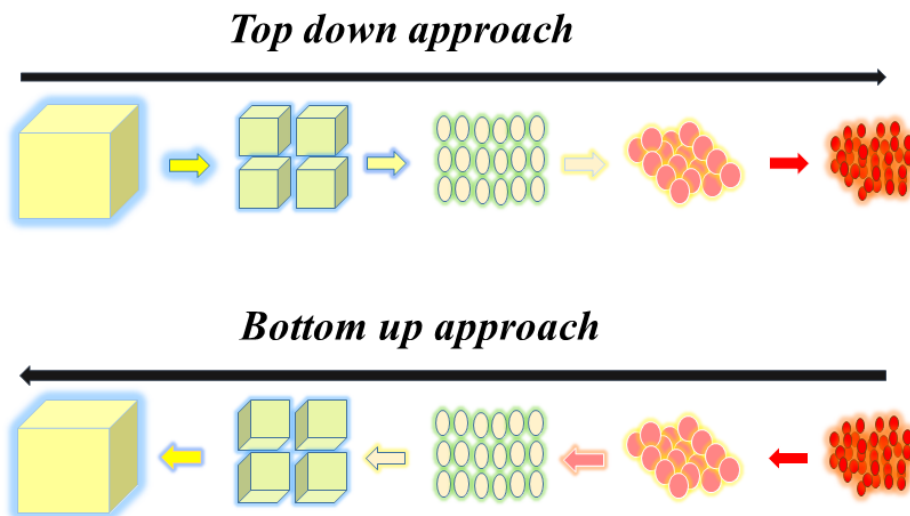
Fig. 3.1. The schematic diagram for the top-down and bottom-up approached for the synthesis of nanomaterials.

The top-down approach follows the route of size reduction of bulk material and its transformation into nanomaterials. This approach includes grinding, crushing and milling large materials and makes them small. This approach is economical and has been widely used to synthesize nanomaterials. But this approach has the drawback that it cannot prepare the NPs

with uniform shape and size. Even after a large consumption of energy, it is challenging to obtain small particles with uniformity. The bottom-up approach follows the route of starting from an atomic scale and then combining the atoms, combining their clusters and finally building up a required nanomaterial. This approach is preferred compared to the top-down approach as this approach can synthesize nanomaterials having a uniform shape, size, and particle distribution. So bottom-up approach plays a significant role in the fabrication of nanomaterials and nanostructures.

3.1 Different Synthesis Methods:

Different synthesis techniques fall in the category of top-down and bottom-up approaches. Various synthesis methods are classified and represented in Fig. 3.1 and all these methods are briefly discussed below:

Fig. 3.2. List of methods adopted for the synthesis of nanomaterials: physical methods, chemical methods, biological methods.
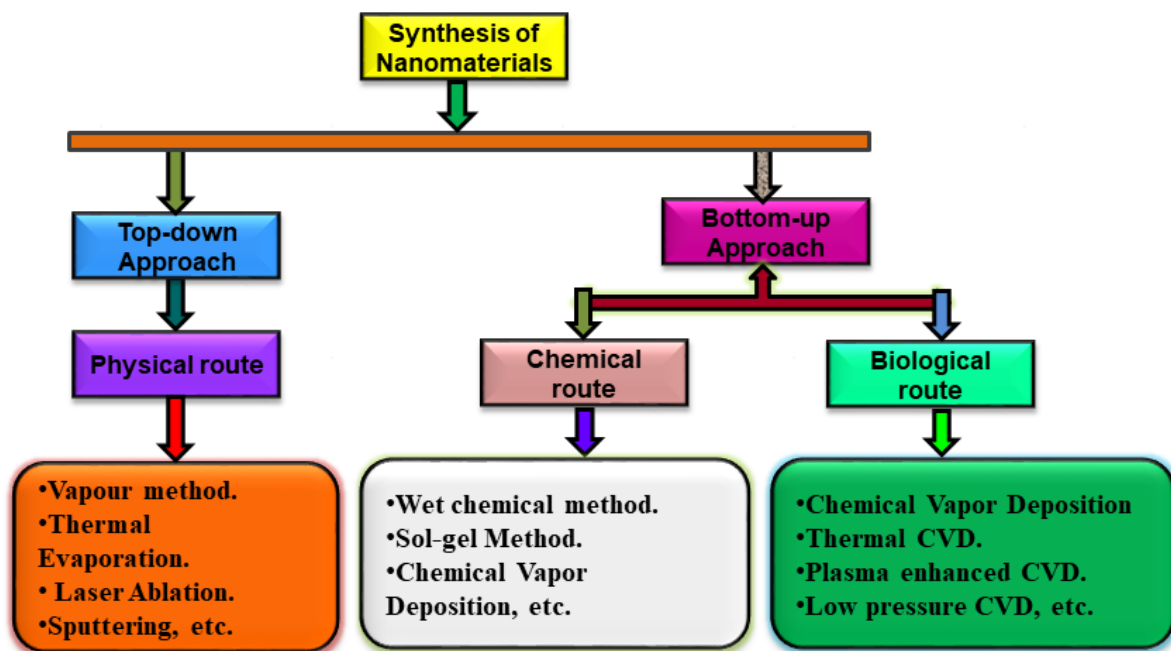
3.2 Physical Methods:

When physical techniques are used to synthesize nanomaterials, we call them physical methods. Based on top-down and bottom-up approaches, these methods are further divided into two categories:

Vapour Methods: In Vapour methods, the entire method in a vacuum chamber. Different techniques adopting top-down and bottom-up approaches fall under this category. Some well-known techniques are discussed below:

Thermal evaporation: This technique falls under the bottom-up approach. This technique is most widely used for making thin films of NPs. This technique is very simple from its instrumentation point of view and also it is cost-effective as compared to many other techniques. The properties of the prepared thin film depend upon inert gas pressure, the distance between source and substrate, evaporation rate and gas composition.

Ion implantation: It is a technique that is performed at a low temperature. In this technique, the ions of the source material are accelerated onto the target material. These ions change the physical, chemical and electrical properties of the target material. This technique is used to fabricate semiconductor devices.

Mechanical Methods:

Ball milling: This process falls under the top-down approach. It involves controlled mechanical attrition of a material to convert it to small NPs in powder form.

3.3 Chemical Methods:

By using chemical methods to synthesize NPs, the size of NPs can be controlled. The method involves the chemical reactions between the constituent materials in a suitable solvent. As all

chemical reactions take place in a solvent, these techniques are called liquid phase techniques. Brief descriptions of some famous chemical methods are discussed below:

Wet chemical method: In the wet chemical method, the suitable salt of the material called precursor is added to the appropriate solvent. The reaction occurs under the controlled temperature and pressure and at the end, non-soluble precipitates are obtained, giving the desirable NPs. Surfactants are used in this technique to maintain the separation between NPs formed. After drying in the vacuum, NPs are obtained. Some polymers or biomolecules are used as reducing agents as well as stabilizing agents in this method.

Sol-gel method: This is one of the most commonly used techniques to synthesize NPs. It is a colloidal chemistry technology that provides NPs with a novel, pre-defined properties at a low process cost. This technique is the mixture of two names, sol and gel. Sol is simply a colloidal solution made of solid particles with a few hundred-nanometre diameters and is suspended in the liquid phase. The main benefit of the sol-gel process is the high purity and uniform nanostructure of synthesized NPs.

3.4 Biological Methods:

This is a green method (i.e., microbial enzymes or plant phytochemicals are used for chemical reactions). Enzymes extracted from microorganisms (bacteria, fungi, yeast) and phytochemicals extracted from plant tissues (leaves, stems, roots) react with metal salts and under the controlled reaction mechanism, NPs are obtained in powder form. The advantage of using biological methods is that they help to synthesize eco-friendly NPs. The size, shape, and nature of those NPs can be altered by varying pH, temperature, and nutrient media.

3.5 Hybrid Methods:

Chemical Vapour Deposition (CVD): This method involves chemical reactions or dissociation of gaseous reactants in a medium that contains a substrate activated by heat, light, or plasma. These chemical reactions are followed by the formation of a stable solid product. The product is obtained as powder, a coating, or as a single crystal. There are three types of CVD techniques.

Thermal CVD, Plasma enhanced CVD, and Low-pressure CVD

Chapter 4

4.1 Characterization Technique:

This section outlines the processes characterization technique of bare and doped ZnO nanoparticles (NPs). A concise description of the principle, operating and experimental setup of the numerous experimental methods exercised in the present research to study the structural, morphological, optical, and magnetic properties of the processed samples are represented with suited figures. Following characterization techniques are listed below, which are used to analyze samples and results based on these data.

4.1.1 Thermogravimetric Analysis (TGA). **4.1.32** X-ray diffractometer (XRD).

4.1.3 Scanning Electron Microscope (SEM). *4.1.3* Energy Dispersive Spectroscopy (EDS).

4.1.5 UV-vis spectrometer. *4.1.6* Spectrofluorometer.

4.1.7 Raman Spectrometer. *4.1.8* Lifetime spectrometer.

4.2 Thermogravimetric Analysis (TGA):

The TGA of the as-prepared nanocomposites is performed with a constant heating cycle of 10 degrees/min to examine their thermal stability. It is systematically carried out using TGA apparatus with model TGA 4000 by Perkin Elmer. TGA represents the thermal degradation of the prepared nanocomposites in terms of their mass loss during heating from room temperature (28 ^{0}C) to the desired high temperature (600 ^{o}C/800 ^{o}C). This measurement provides information about the chemical phenomenon (thermal decomposition) as well as a physical phenomenon (phase transition).

Fig. 4.1 Photograph of TGA instrument in DTU.

The endothermic or exothermic process of the material was recorded concerning the reference material. The grown crystals were uniformly crushed into a fine powder using a mortar pestle and used for analysis. Thermal analyses were examine by using Perkin Elmer for the temperature range 30ºC to 300 ºC in a nitrogen atmosphere at a heating rate of 10 ºC. The melting point, decomposition point, thermal stability, polymerization, purity and reactivity of material were identified by TG-DTA analysis. The photograph of the TG/DTA instrument is given in Figure 4.1 from the Delhi Technological University (DTU), Delhi.

4.3 X-ray Diffraction Method (XRD):

X-ray powder diffractometer (XRD) is a speedy logical technique fundamentally used for level conspicuous verification of a crystalline substance and can give information on single-cell approximations. The analyzed matter is accurately grounded, homogenized, and the average composed and setup of mass material is resolved.

Fig. 4.2 X-ray Diffractometer [Model: Bruker's D8 Discover] in DTU.

Basic Concept: Max von Laue, in 1912, found that substances were having crystallites popularly travel through as 3-D diffraction grindings for X-shaft ranges like the dislocations of planes in a cross-sectional circle. Currently, X-shaft diffraction is regarded as a typical way for the cross-examination of precious stone structures and nuclear spacing as shown in Fig. 4.2. Depending on productive interruption of paths of monochromatic beams and the standard substances, these beams are created by a CRT, which are kept to deliver monochromatic energies; generally, they are collimated so that they can strike and synchronized with the example. The relationship between the originating beams with the example produces impedance (and a diffracted shaft) fulfilling the Bragg's Law conditions,

$$2d \, \mathrm{Sin}\theta = n\lambda \tag{4.1}$$

This hypothesis tries to connect the wavelength of emission radiation to the diffraction values observed and the cross-sectional divisions of a crystalline standard. Upon studying the 2 theta angles and comparing them with the standard ZnO samples, we get to know about the various diffraction values obtained. This technique helps us in evaluating layer separations present inside the material. We can even determine the various domains present inside the sample, their

homogeneity. The average width regarding their crystallinity can also be calculated from the peak values obtained in the XRD pattern. While keeping all these, we generally use CuKα1 and CuKα2 as standards for wavelengths, which help calculate various mathematical formulas [83], and even help determine the FWHM of the sample [84].

4.3 UV-Visible-NIR spectrophotometer:

Depending on the different qualities of synthetic mixes present in nature, they carry on diversely when electromagnetic waves fall on them. They either reflect, assimilate, or transmits a specific area of recurrence or wavelength. A spectrophotometer (Fig 4.3) is an investigation system that causes us to decide how much a material transmits or assimilates a specific area of electromagnetic wave. By and large, there are two exceptionally well-known kinds of the spectrophotometer. One is atomic discharge spectrophotometry and the other is nuclear absorption spectrophotometry. This system or gear fundamentally figures the number of photons ingested when the example arrangement is exposed to the way of these photons. Each compound substance has a specific wavelength which it retains and hence this strategy causes us to discover the substance's absorbance pinnacle [85]. Contingent on the scope of wavelength that is utilized, it very well may be portrayed in two sorts:

Fig. 4.3 UV-Vis-NIR Spectrophotometer (Model: Perkin Elmer 750 LAMBDA) [86].

UV-Visible spectrophotometer: This operates in the ultraviolet range (190nm- 400nm) and visible range (400nm-700nm) of the EM radiation spectrum. IR spectrophotometer: The

operating range is the infrared region (700nm-3200 nm) of the EM radiation spectrum and the schematic representation UV-Vis-NIR Spectrophotometer as shown in Fig. 4.4.

Principle: The Beer-Lamberts hypothesis expresses that the absorption of a material in the form of solution is straightforwardly corresponding to the grouping of the remaining species in the mixture and in the distance they traverse. Accordingly, for a standard mean way length, a UV-Vis spectrometer can be utilized to decide the amount of the absorbing material in the prepared sample. The absorption changes with the amount of the sample present in the solution. This can be taken from standards (tables of molar annihilation coefficients), or all the more precisely, decided by an adjustment bend [87].
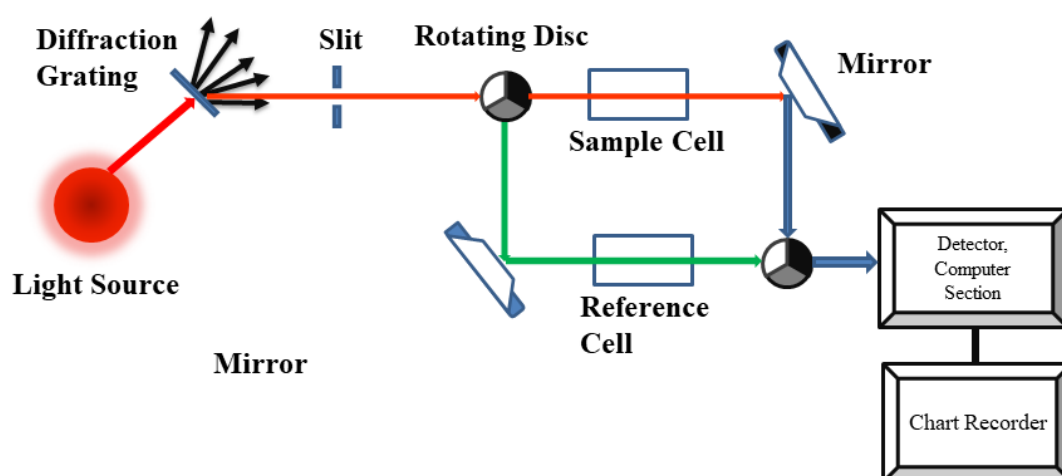
Fig. 4.4 Schematic diagram of UV-Vis-NIR Spectrophotometer.

Reference and sample compartments: These are little cubical quartz compartments. They are frequently structured, so the photons traverse a separation of 1 cm along the given direction of the sample. The testing compartments contain an answer of the sample solution we are trying - generally exceptionally weak. The material on which the sample is dissolved is picked not to retain any critical measure of photons in the range of wavelength extend (200-800 nm). The standard compartment involves the unadulterated spectrum of pure solvent i.e. used.

Demodulator and the PC: The indicator changes over the approaching photons into an electrical signal. More the value of the electrical impulse, the more prominent the strength of the photons. For every region of light wavelengths traversing along the spectro-photometer, the force of the photons traversing through the standard compartment is estimated. This is generally alluded to as I_0, i.e., I for Intensity. The power of the photons traveling towards the example compartments is additionally estimated for that range or region – taken from the image, I_0 If I am not very close to the value of I_0, at that instant the sample has assimilated a region of the photons. A rightful analysis and calculations are then performed on the desktop to revise the value so that it can be standardized for everybody using the standard as absorbance - given the graph, A. For reasons which will progress toward becoming clearer if we complete a touch of hypothesis on another value, the connection among and the two powers is given by:

$$A = log_e \left(\frac{I_0}{I} \right) \tag{4.3}$$

Over the vast majority of the outlines, we will encompass over, the value of absorbance traverses over 0 to 1, however it can even attain a higher value than that. A value of zero at some wavelength implies that no photons of that given frequency have been retained. The powers of the example and standard shaft both are equivalent; therefore the proportion I_0/I is one. Log10 of one is zero. An absorption value of one appears when 90 percent of the photons at that range has been assimilated - which implies that the power is 10 percent of the photons traversed some way or another be. In that case, I_0/I is 100/Io (=10)[88].

4.7 Spectrofluorometer:

A spectrofluorometer is an instrument that takes resources of fluorescent properties of few mixes to contribute data concerning their focus and synthetic environment in an example. Some excitation wavelength is picked, and the discharge is perceived either at an absorbing

wavelength, or a sweep is executed to take note of the power versus wavelength, for example, outflow spectra [89].
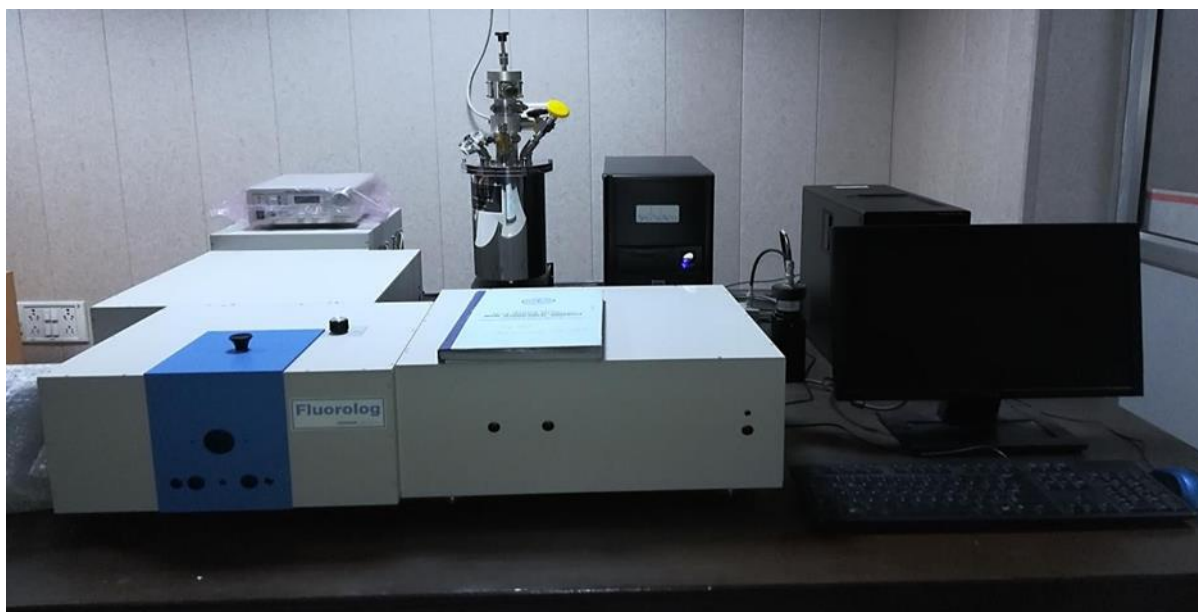

Fig. 4.5 Fluorolog-3, Horiba Scientific Inc. [90].

With most spectrofluorometers, it is practical to watch both excitations as well as emission spectra. An excitation range thoroughly relies upon the outflow force since it is estimated at a solitary emanation wavelength. Alternately, a discharge range absolutely relies upon the excitation wavelength. Such produced spectra can be spoken to on either a wavenumber scale or a wavelength scale. Normally, emanation/PL of a given vitality can appear as far as its wavelength (λ), wavenumber or recurrence (v). The general units for wavelength are in nanometers and wavenumbers. For an ideal instrument, the unequivocally recorded discharge spectra would show power radiated at every wavelength or the photon outflow rate over an interim of wavelength settled by the cut expansiveness and scattering of the emanation monochromators (Fig. 4.5). Similarly, at every excitation wavelength, the excitation range demonstrates the general discharge of the fluorophore. For most fluorophores, the discharge/PL spectra and quantum yields are isolated from the excitation wavelength. Accordingly, the excitation range of an example arrangement can be cover on its retention range. In any case,

such similar retention and excitation spectra are infrequently watched in light of the fact that the excitation power is unmistakable at every wavelength. Indeed, even under ideal conditions, such closeness of the excitation and retention spectra requires the presence of just an exceptional sort of fluorophore and the nonappearance of other confusable variables.
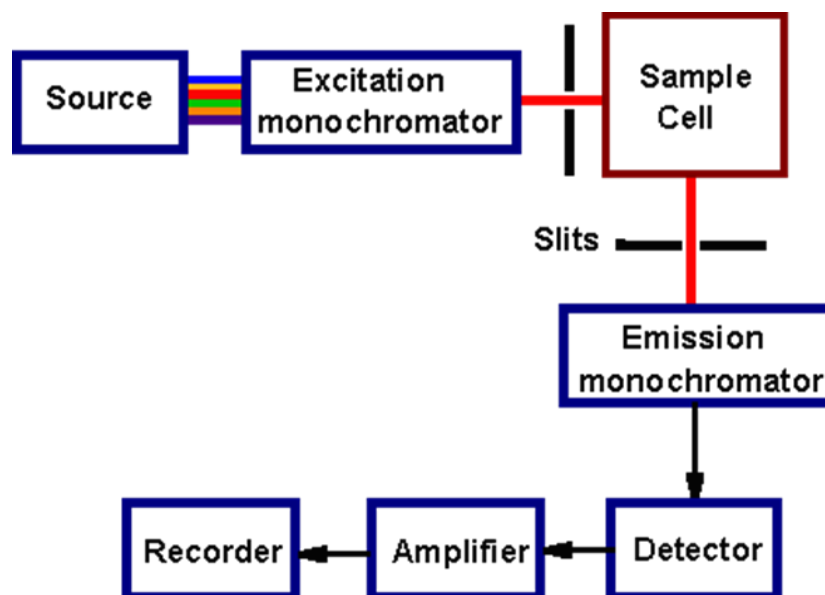

Fig. 4.6 Schematic representation of spectrofluorometer.

Outflow spectra recorded on particular instruments can be unmistakable because instruments are wavelength touchy. The spectrofluorometer (Fig. 4.6) comprising xenon circular segment lights as a light wellspring of 450 W generally helpful on account of their tremendous power at all wavelengths running from 200 nm, double monochromators to world-class both the excitation and discharge wavelengths. Moreover, curved gratings are utilized by these monochromators, produced by holographic intends to decreasing stray light. An example area with a cuvette holder and a photomultiplier tube (PMT) for the discovery of fluorescence and after that deliberate it with appropriate electronic gadgets. The yield is commonly spoken to in the graphical structure [91].

4.8 Raman spectroscopy:

It gives information on molecular vibrations, which can be applied for molecular structure measurement, sample classification.

Raman Effect: When a monochromatic light beam interacts with a substance, a small amount of radiation energy will be scattered. The scattered light contains mostly radiation of incident frequency which is called Rayleigh scattering as shown in Fig. 4.7. A small amount of scattered light will have a frequency greater or lesser than the incident frequency and this process is called Raman scattering (Raman Effect)[92].

Principle of Raman Spectroscopy:

The principle of Raman spectroscopy is "inelastic scattering of light". Generally, when the photons emitted from the laser is made to fall on the sample, they are absorbed by the molecules either atom in the specimen and are emitted back. The back emitted photons may have experienced a change in their frequencies, which is Raman inelastic scattering.
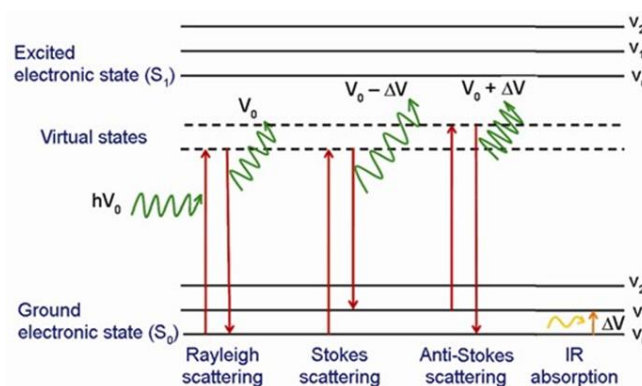
Fig. 4.7 Rayleigh and Raman

Their frequency may get changed higher or below connected to the beginning monochromatic frequency. This shift offers the data of vibrational, rotational and additional lower frequency.

Raman spectroscopy is a technique for investigating 'solid', 'liquid' and 'gaseous' samples. In this method, when monochromatic radiation having wave number (v_0) is incident on the dust-free sample, the majority of the radiation is transmitted without change, along with some

inelastically scattered radiation. But scattered light has a frequency in the form of new wave numbers $\upsilon = \upsilon_0 \pm \upsilon_m$.

Fig. 4.8 Block diagram of Raman Spectrometer

More often, in a molecular spectroscopic system, the wavenumber υ_m is found to be predominantly in the ranges linked with transitions among vibrational, rotational a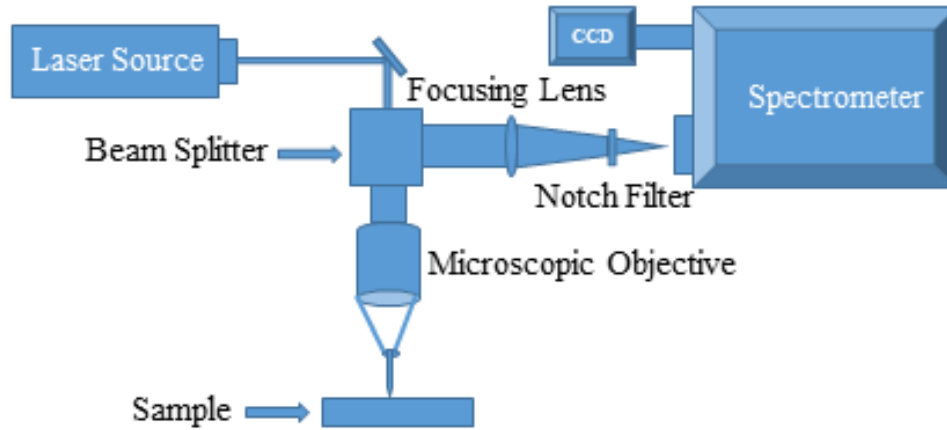nd electronic levels. Applications of Raman spectroscopy are extensive in the fields of physical, chemical, biological and medical sciences [93]. The UV-Vis-NIR range laser beam is employed as the source to illuminate the sample. Raman system usually has the following most important parts as represented in the Fig. 4.8.

4.9 Field Emission Scanning Electron Microscopy (FESEM):

The FESEM is a high-resolution microscope that uses electrons for interacting with samples to get data about surface morphology, orientation, and synthetic composition of materials that make the sample. FESEM uses a field emission gun (FEG) to generate the high-energy electron beam where the ordinary SEM uses thermionic emission. The principle of FESEM is the detection and picturization of secondary and backscattering electrons as an effect of the interaction electron beam and with sample surface [94]. Necessary apparatuses of SEM are

Sample Stage, electron source (FEG), Magnetic lenses, Detectors (for all released signals), and Display / Data output devices as shown in Fig. 4.9.
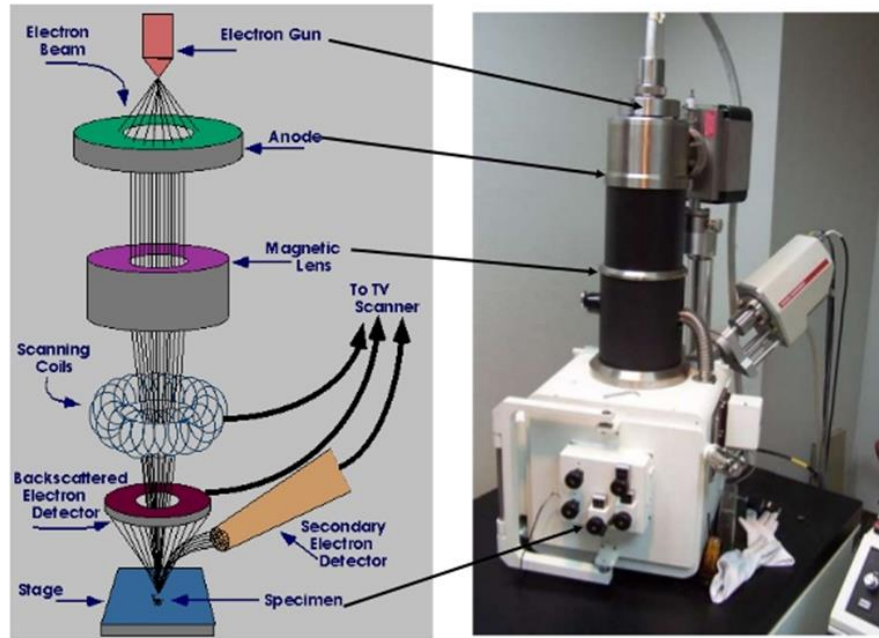

Fig. 4.9 Block Diagram of Scanning Electron Microscope with SEM with EDS.

Infrastructure Requirements:

Vacuum System, Power Supply, Cooling system, and Vibration-free floor are the main requirements. In FESEM, FEG emits a high-energy electron beam that travels through the high vacuum column. These primary electrons subsequently travel down via a succession of magnetic lenses intended to focus the electron beam into an incredibly fine spot. This accelerated electron beam bears a considerable amount of kinetic energy. The sample data are visualized using a recording device or cathode ray tube (CRT). The scan coils show the way to the objective lens. Thus the electron probe scans in raster from corner to corner of the specimen (to form an image, the modulated intensity is recorded). While electron sample interactions occur, this energy gets dissipated as a mixture of signals created when the incident electrons get decelerated in the sample as represented in the Fig. 4.10 [95]. These signals contain secondary electrons (SE) [denotes the morphology of samples], Backscattered electrons (BSE),

(illustrate the contrasts in the composition of multiphase samples), characteristic X-rays, Auger electrons, Cathodoluminescence (CL) and heat.
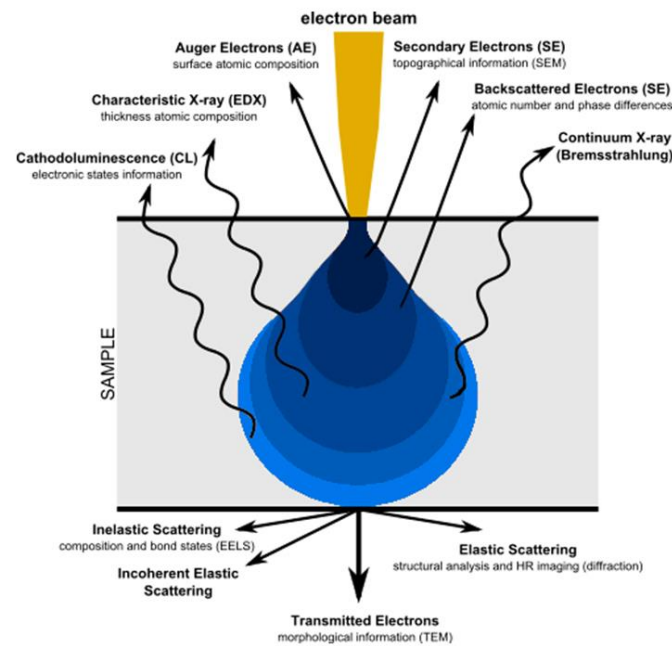
Fig. 4.10 Illustration of the interaction of electrons with the sample surface.

4.10 Energy Dispersive X-Ray Spectroscopy (EDS):

EDS is a systematic method employed for the compositional investigation of the samples. This method is based on analyzing samples within interactions among electromagnetic radiation, including samples. Analyzing these X−rays emitted by the sample provides details regarding the elemental composition of the samples. Without excitation, an atom inside the sample has electrons at the ground state with discrete energy levels. A high-energy ray of electrons is sent to hit the specimen, which is to be examined. Subsequently, an electron is excited from an inner shell, then got ejected from the shell while leaving an electron-hole in that place. This position is eventually occupied by an outer shell higher energy electron. This kindles the characteristic X−rays emission from the sample [96]. The variation in energy within the high and low-energy shells may determine the amount of energy of the released X−rays as shown in Fig. 4.11.
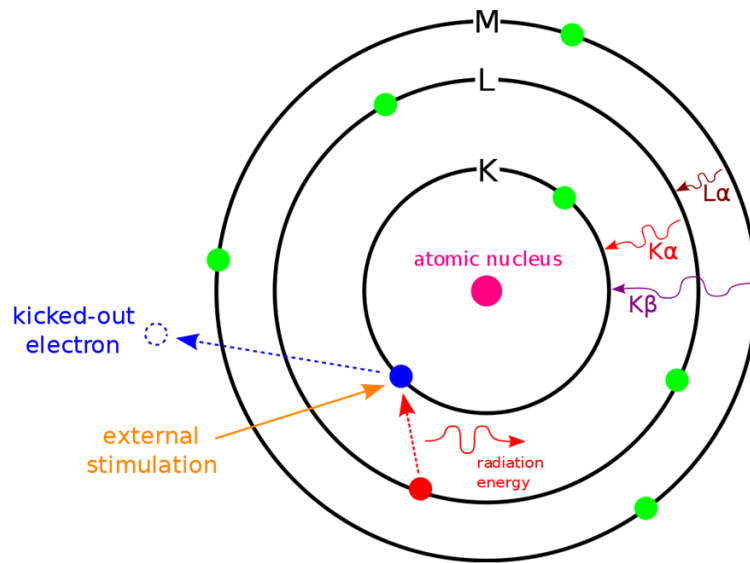
Fig. 4.11 Principle of EDS.

Specifications:

Make and model: FEI, Quanta 3D and FEI, Quanta FEG 200 Resolution: 1.2 nm gold particle separation on a carbon substrate Accelerating Voltage: 0.2 to 30 kV, Magnification: up to 2, 50,000 X.

4.12 Time correlated single photon counting (TCSPC):

The lifetimes value were estimated operating the TCSPC System on Horiba Jobin Yovn, DeltaFlex equipped with DeltaDiode (Pulse Width: <1ns), with PPD detector [105]. The data were fitted with the least squire method [97]. The block diagram of lifetime measurements system as display in the Fig. 4.12.
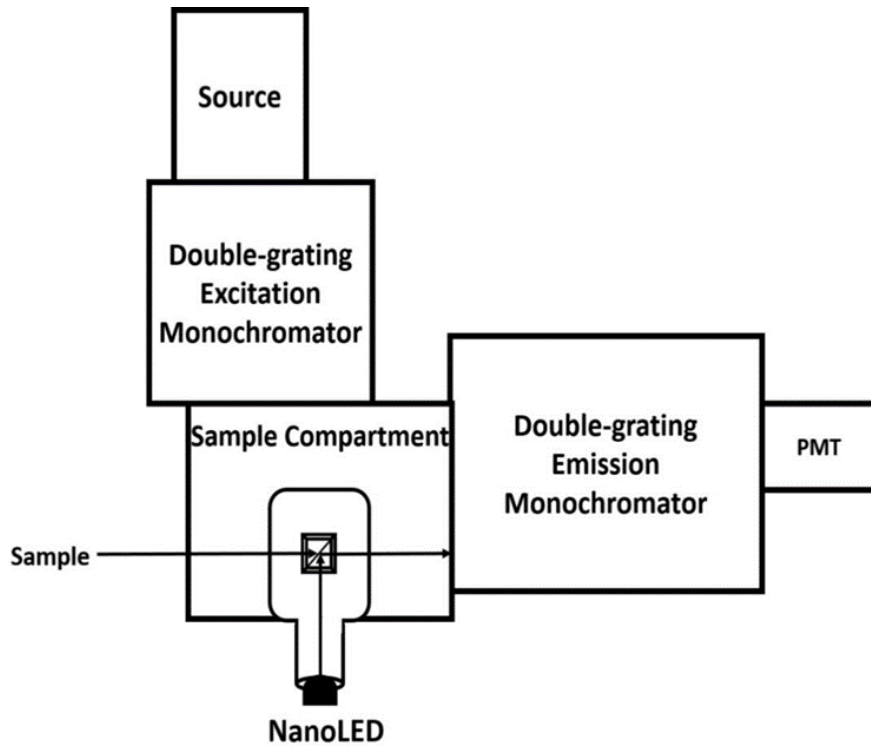
Fig. 4.12 Block diagram of lifetime measurements system.

The well-being fit was estimated by chi-square with the Durbin- Watson parameters, furthermore visual observations of the fitted line, residuals, and autocorrelation functions. The average lifetime (τav) with amplitude (Ai) and lifetime τi, i =1, 2, 3 were calculated using the following equation [107].

$$\tau_{av} = \sum_i \frac{A_i \, \tau_i^2}{A_i \, \tau_i} \qquad (4.4)$$

Chapter 5

Synthesis of ZnO NPs using Sol-gel Method and their Applications[$]

5.1. Introduction

The material zinc oxide (ZnO) has played a vital role in various sectors in the ever-growing research field. The ZnO is (II-IV) semiconductor material, possessing wide bandgap energy of 3.3 eV at ambient temperature and pressure with large excitons (60 meV) [98–100]. It is found in two common polytypes, i.e., cubic zinc and blende hexagonal Wurtzite. The Wurtzite phase having tetrahedral coordination, which exhibits sp^3 covalent bonding, is the most stable phase at favorable conditions. It has outstanding multifunctional material properties, such as high chemical and photostability, a wide range of radiation absorption, wide bandgap, cheap and non-toxic. In past decades, researchers paid serious attention to the ZnO for its magnificent properties, which could be employed in various applications like in spintronic, optoelectronic, piezoelectric, and photochemical materials [101,102], superconductors [75], photocatalyst [103,104], magnetic [75,105], light-emitting diodes [106] and biological applications [107].

Various techniques were used to process different types of ZnO nanostructures including, sol-gel technique, co-precipitation, chemical vapour deposition, hydrothermal method, *etc.* [80,108–113] and solved the purposes. The sol-gel approach proved to be the most favorable because it is very pocket-friendly, facile, and produces a scalable amount of nanoparticles. The properties and the application of ZnO depend primarily on its shape, size, and structure. The spherical nanostructures of ZnO are mainly exploited for their photocatalytic activities [114].

In this era of industrialization, the increasing demand for products like textiles, toiletries, healthcare, food, beverages, and other industries had led to the release of highly toxic organic compounds like dyes untreated into the water bodies. This causes the destruction of natural reserves of water (rivers, lakes, etc.), which has a long-lasting adverse effect on humanity and the aquatic ecosystem. One such commonly used synthetic dye is the Congo red (CR) dye, an anionic azo and water-soluble red dye used majorly in textile and leather industries. The presence of a meagre amount of the compound could lead to chronic carcinogenic diseases in human beings. This industrial pollutant can cause severe environmental effluences such as water pollution, destruction of water plants, and extinction of aquatic life because of the colorization of the water bodies by the dye extracts discarded directly to rivers through sewage.

Over the past few decades, a tremendous increase in the efforts has been employed for the enviro-friendly ways to remove the dye's waste from the water through photocatalytic activity [77]. Many different photocatalytic materials have been developed and used for eliminating CR from sewage waste. The photocatalytic activities of metal oxide semiconductors (MOS) are preferred because of their efficient adsorption and photocatalytic properties [115]. When the MOS is transformed into nanoparticles, they exhibit unique physicochemical and biological properties because of the enhancement in surface area to volume ratio.

The ZnO had always been the first choice for photocatalytic decomposition of organic contaminants [116]. The pristine ZnO nanomaterials have been produced via the sol-gel method and employed directly to decompose the congo red dye in the current work. The elaborated structural, morphology, optical study have been investigated for the ZnO-based photocatalytic activity.

5.2. Experimental details:

5.2.1 Materials and Equipment's section:

All the high purity chemicals were of analytical grades, such as zinc acetate dihydrate $((CH_3COO)_2Zn).2H_2O)$ bought from Sigma-Aldrich with a purity of 99.99%. Sodium hydroxide (NaOH) has been purchased from the CDH and used without any further purification. The de-ionized (DI) water (specific resistivity: 18.2 MΩ × cm) was used as the medium.

5.2.1 Preparation of ZnO Nanoparticles:

4.243 gm of zinc acetate dihydrate powders were dispersed in 100 ml DI and then kept on the magnetic stirrer (900 rpm) for 30 minutes. Simultaneously, 4 gm of NaOH was mixed with 50 ml of DI and kept on the magnetic stirrer (800 rpm) for 15 min. We had obtained the two clear solutions from the above procedure then the NaOH solution was mixed dropwise in the zinc acetate solution under vigorous stirring for 1 h. The precipitate (white color gel) was formed and left to settle. The residue was washed and filtered four times with DI and ethanol (1:1). It was heated in an oven at 60 °C for 120 min to remove wetness from the precipitate. The dried NPs were calcined at 300 °C for 180 min to get the desire ZnO NPs. The synthesis procedure of ZnO and doped ZnO is systematically represented in the scheme. 5.1.
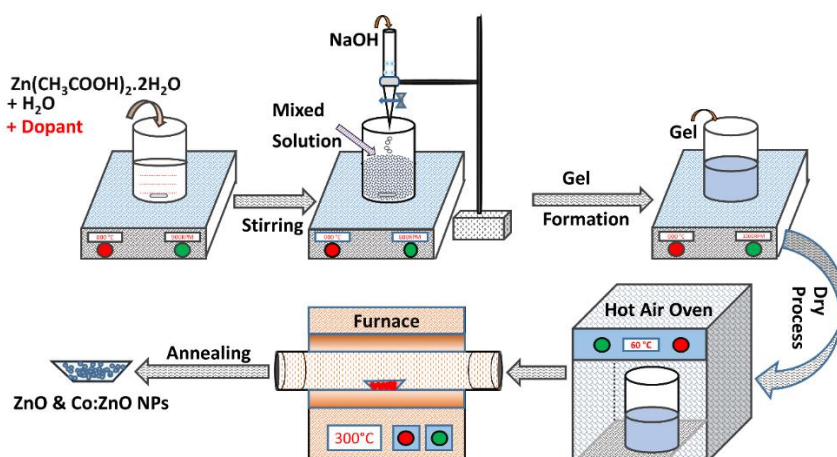
Scheme 5.1. Schematic representation of the synthesis of pure ZnO and Co-doped ZnO.

5.2.3 Material characterization techniques:

X-ray diffraction (XRD) analysis by Bruker 8D Advance having Cu Kα (1.54 Å) source radiation with an accelerating voltage of 0.04 MV and current of 0.02 Am. The absorption and reflectance spectra were analyzed with a spectrometer (Perkin Elmer, dual-beam Lambda-750, UV/VIS/NIR). The Photoluminescence (PL) spectra analysis with the Spectrofluorometer Horiba Scientific Inc., USA (Fluorolog-3), equipped with double grating both at emission and excitation monochromators [117]. The structural morphology and elemental compositional of all the samples by using the Field Emission Scanning Electron microscope (FESEM) and energy-dispersive X-ray spectrum analysis (EDAX), (SEM, ZEISS Microscope MA15/18 and EDS 51N1000 – EDS System). VSM (Vibrating Sample Magnetometer) was used to examine the magnetic nature of the produced ZnO NPs.

5.3. Results and Discussion:

5.3.1. X-ray diffraction analysis:

The X-ray diffraction patterns depict the structural information about the ZnO, which attributes to the diffraction peaks at Braggs angle of (2θ) 31.76°, 34.42°, 36.25°, 47.53°, 56.59°, 62.85°, 66.374°, 67.94°, 69.08°, that correspond to (100), (002), (101), (102), (110), (103), (200), (112), (201) crystal plane, respectively as shown in Fig. 5.2.
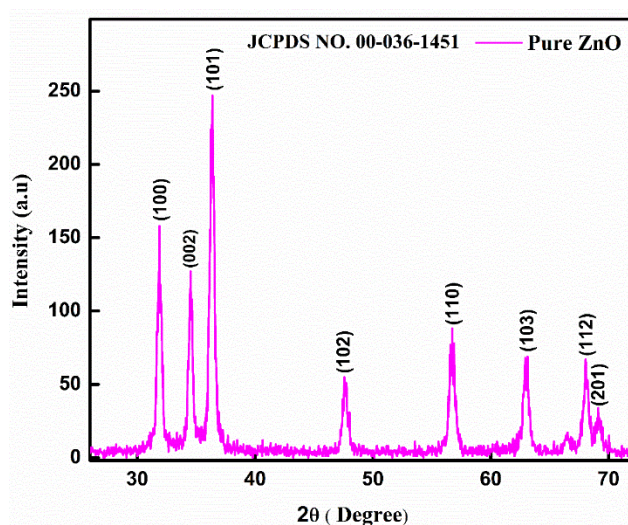

Fig. 5.2. X-ray diffraction pattern of ZnO NPs**.**

The peaks demonstrated ZnO nanoparticle formation with hexagonal Wurtzite crystal structure, following the standard spectrum of JCPDS Card No. 00-036-1451. The diffraction patterns indicate no impurities exist in the standard hexagonal Wurtzite structure [118,119]. Using Scherrer's formula (Eq. 5.1), the average crystallite size was estimated from the ZnO peaks ((110), (002)) [83,120].

$$D = \frac{0.9\lambda}{\beta \, \cos\theta} \tag{5.1}$$

where λ is the X-ray source wavelength (CuKα having $\lambda = 0.154$ nm) and 'β' is the full width of the angular peak at the half maximum (Radian), θ is the Bragg's diffraction angle. Using Eq. 5.2, where a=b and c are the lattice parameters of the ZnO nanoparticles, calculated to be 3.245 and 5.196 Å [121].

$$\frac{1}{d_{hkl}^2} = \frac{4}{3}\left(\frac{h^2+hk+k^2}{a^2}\right) + \frac{l^2}{c^2} \tag{5.2}$$

Where the miller indices (h,k,l), inter-planar spacing 'd'. The values of 'a' and 'c' were calculated by (110) and (002) crystal planes corresponding to the peak position of 56.59° and 34.42°. The atomic packing factor (APF) ratio (c/a) and the cell volume of the lattice of the ZnO in the tetrahedral coordination were calculated to be 1.60 and 47.38 (Å)[3,] respectively [122]. The bond length of all the samples estimated using Eqs. 5.3 and 5.4 came out to be 1.97 Å [123].

$$u = \left(\frac{a^2}{3c^2} + 0.25\right) \tag{5.3}$$

$$L = \sqrt{\frac{a^2}{3} + \left(\frac{1}{2} - u^2\right)^2 c^2} \tag{5.4}$$

The positional parameter 'u' (~0.38) is calculated from Eq. 3. The ionic characteristics and distortion of all the NPs were identified by positional parameters [124,125]. The crystallite size is inversely proportional to the dislocation density (δ) and how much defect exists in the NPs. The dislocation density (2.5×10^{-3} nm^{-2}) was determined by using Eq. 5.5 [126],

$$\delta = \frac{1}{D^2} \tag{5.5}$$

Where 'D' is the crystallite size obtain from the XRD results. Variation of crystallite size

depends on $\frac{1}{Cos\theta}$, while strain with tanθ, and both, in turn, depend on diffraction angle θ.
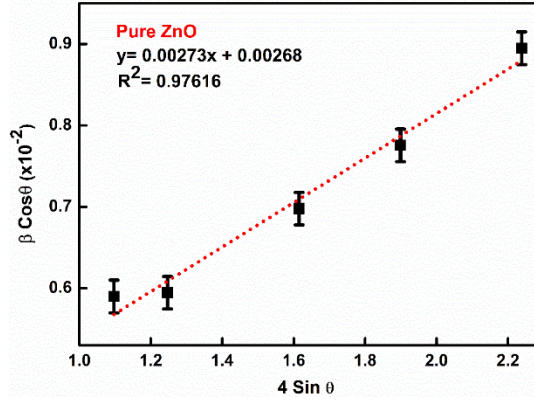
Fig. 5.3. The W-H plot between βcosθ *vs.* 4sinθ of synthesized ZnO NPs.

The crystal imperfection and distortion in powder causes strain-induced broadening calculated

using Williamson-Hall (W-H) method Eq. 56 [127],

$$\varepsilon = \frac{\beta Cos\,\theta}{4\,Sin\theta} \tag{5.6}$$

The microstrain (ε), dislocation density (δ) of the nanoparticles is more prominent as compared

to the crystallite size (D). It may be because of the lattice contractions [120,128]. The W-H plot

of synthesized NPs $\beta cos\,\theta$ (y- axis) vs $4\,sin\theta$ (x- axis) are presented in the Fig. 5.3. The degree

of distortion 'R' was evaluated by Eq. 7, where a, c are lattice constants.

$$R = \frac{2a\,\,(2\div3)^{1/2}}{c} \tag{5.7}$$

To verify all the sample's structure is an ideal Wurtzite structure, the degree of distortion value

should be unity [129]. The calculated R-values were approximately found to be 1.02.

5.3.2. FESEM images and EDAX spectrum:

The FESEM images of the nanoparticles are shown in Fig. 5.5(a) and display the particles are

in granular nature, spherical and rod-like mixed-phase (hexagonal and spherical)

[108,130,131].
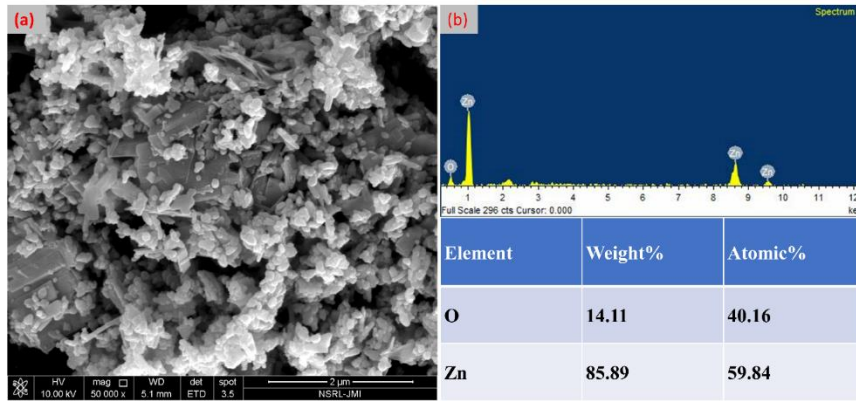
Fig. 5.4. FESEM image (a) and EDAX spectrum (b) of the ZnO NPs.

The particle size of the ZnO was measured and found to be 54 nm. The elemental compositional analysis was confirmed by the EDAX spectroscopy of the NPs, as shown in Fig. 5.4(b), which depicts that the Zn and O elements are the leading entities in the sample of ZnO NPs and there were no other fundamental peaks observed in the EDAX spectra.

5.3.3. UV-vis absorption and diffuse reflectance spectra:

The absorption and reflectance spectra of ZnO NPs were explored in the wavelength range of 200 to 800 nm at ambient temperature and pressure, as presented in Fig. 5.5 (a,b).
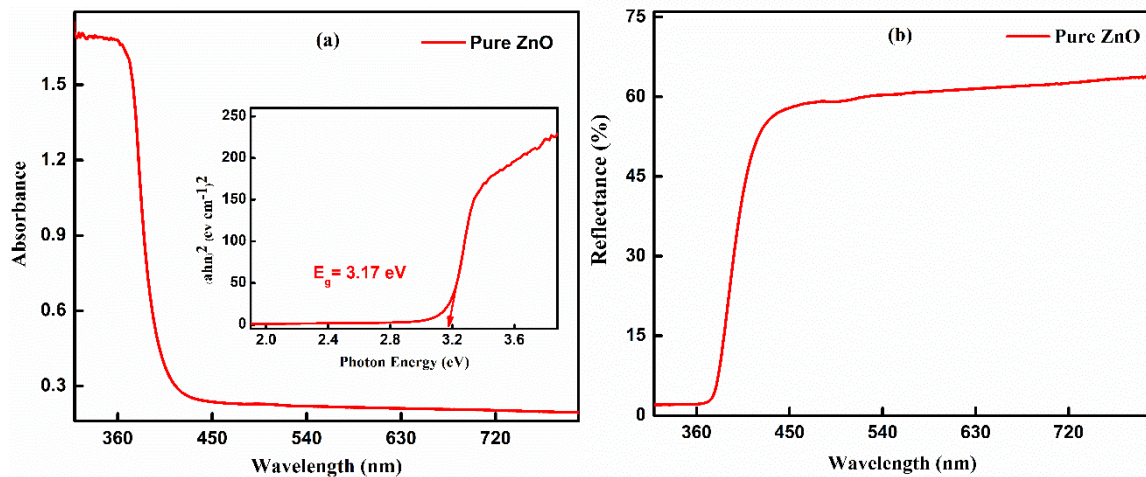
Fig. 5.5. The absorption spectrum along with the Tauc plot (inset) corresponding to the direct bandgap (a) and diffuse reflectance spectrum (b) of the ZnO NPs.

Using the well-known Tauc plot relation (Eq. 5.8), the calculated optical bandgap energy is 3.13 eV [132,133]. The plot of '$Ah\nu$ vs. $h\nu$' for pure ZnO NPs is shown in Fig. 5.5 (a).

$$Ah\nu = A(h\nu - Eg)^n \tag{5.8}$$

55

E_g represents the bandgap energy of the specimen, '*A*' is the constant, hv is the incident photon energy, *n* is the transition coefficient and the value of n depending on the inherent characteristics of semiconductor materials [134,135]. The values of n = 1/2, 3/2, 2 and 3 represent the direct bandgap, forbidden direct bandgap, indirect bandgap, and forbidden indirect transition gap, respectively).

5.3.4. Refractive index (RI) analysis:

Nowadays, the modern technology moving towards the design and fabrication section and fabrication of the optoelectronics and integrated circuit (IC, 7, 5, 3 nm) components are as small as possible. Therefore, it is essential to calculate and compare the bandgap and RI of the materials to design and fabricate such sections. Applications of electronic, optical, and optoelectronics of semiconductor materials usually depend on their refractive index and bandgap energy. The energy gap measures the photon absorption threshold, whereas the refractive index measures transparency to the incident photons [136]. To determine the refractive index, many empirical relations were proposed [136–138]. Moss [138] suggested the first relation in 1950 with the known energy gap of semiconductor materials. Five empirical relationships were used to evaluate the refractive index (Eq. 5.9) with the known bandgap (3.17 eV). Suppose the bandgap value of the materials is very small or huge. In that case, the relation [138] is not well suited for the calculation of the RI and fits for the range of the energy gap 0.5 eV < Eg < 3.68 eV of the materials [136].

$$n = \left(\frac{95}{Eg}\right)^{\frac{1}{4}} \tag{5.9}$$

Eq. 5.10 [139,140] validates if the value of energy gap falls in between the range 1.5eV < Eg < 3.50 eV and the theory failed for the values in the region other than this, i.e., if Eg > 6.587 eV and gives negative value [136,139,140].

$$n = 4.084 - 0.63Eg \tag{5.10}$$

The relation (Eq. 5.11) at low and high values of the energy gap [141] provided nearly the same value as obtained from Moss relation. The expression failed when energy gap is Eg < 1.4 eV, however Eq. 5.10 is reliable in the range of 2.0 eV < Eg < 4.0 eV [136,139].

$$n = \sqrt{1 + \left(\frac{13.6}{Eg+3.47}\right)^2} \qquad (5.11)$$

The modified Moss relation (Eq. 5.12), in which the constant value of 0.365 was subtracted from the energy gap and yielded a better result than Eq. 5.9 [142,143]. This relation not valid when bandgap is about 0.365 eV but valid for the range of 1.10 eV < Eg < 6.20 eV [142].

$$n = \left(\frac{154}{Eg-0.365}\right)^{\frac{1}{4}} \qquad (5.12)$$

Kumar and Singh reported by Eq. 5.13 [144] that when the energy gap is at a lower value, its refractive index lies between the Moss [138] and Reddy [49,50] relation. While at a higher value of Eg, it lies below the Reddy relation and higher in Moss relation. The typical reliable rage is 2.00 eV < Eg < 4.00 eV [143,145,146].

$$n = 3.3668(Eg)^{-0.3228} \qquad (5.13)$$

Above all, the relation gives a better result when the energy gap lies between the ranges of 2.0 eV to 4.0 eV. Thus, the refractive index values of the ZnO NPs were calculated from the given above five relations (Eqs. 5.9, 5.10, 5.11, 5.12, 5.13). The refractive index estimated from Moss relation is (2.33) whereas from Kumar & Singh to be (2.32), nearly identical. The highest refractive index of NPs is (2.72) was calculated through the Reddy and Anjayenulu relations [142] while the lowest refractive index (2.08) of NPs by Ravindra et al. [139]. The moderate RI was calculated by Harve et al.[141] is (2.27).

5.3.5 Photoluminescence (PL) spectra:

PL spectra provide information about excited states and their energy and the presence of defects and trap states. The spectral intensity is associated directly with the semiconductors defect density or structural defects [147].
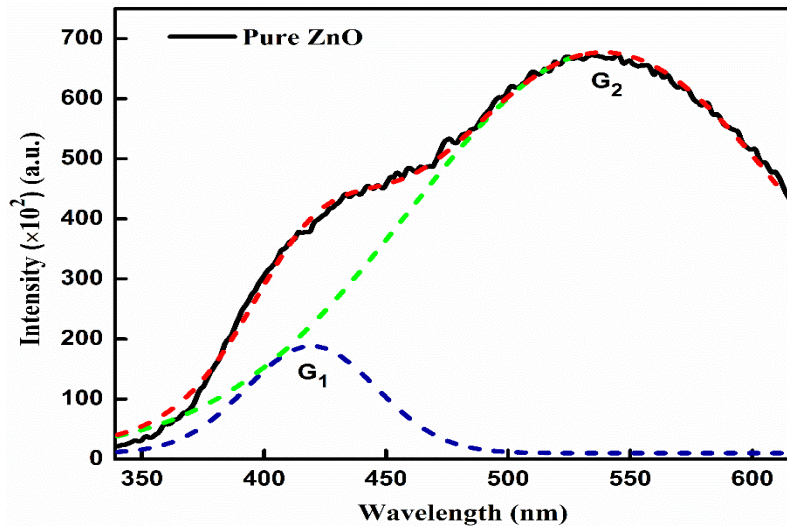
Fig. 5.6. The photoluminescence spectrum (solid red line) of ZnO NPs and G_1 and G_2 Gaussian bands (dotted blue and green line) along with the fitted curve (red dotted line). The excitation wavelength (λ_{ex}) was 320 nm.

The PL spectrum of ZnO NPs has been measured in the wavelength range of 200 to 800 nm at the excitation wavelength of 320 nm at ambient conditions and illustrated in Fig. 5.6. A broad PL spectrum is observed with a band maximum at 540 nm. The Gaussian bands (G1 and G2) well reproduce the PL spectrum. G1 appeared at 434 nm and G2 at 540 nm. These bands are well-matched with the reported values [55-58]. The G1 band, which is located at around 434 nm, originated from the direct bandgap energy, i.e., the recombination of electrons (e^-) from the conduction band (CB) to the zinc vacancies (V_{zn}) [148]

Whereas the relative stronger band observed at 540 nm related to the oxygen vacancies (V_O) and zinc interstitials (Zn_i), or transition from the valence band to the oxygen vacancies (V_O) and zinc interstitials (Zn_i) [149,150].

5.3.6. Magnetic properties:

The magnetic characteristics of the synthesized ZnO NPs were measured at 300 K via a vibrating sample magnetometer. The M-H curve of the NPs exhibited diamagnetic nature, as shown in Fig. 5.7.

Fig. 5.7. M-H curve of ZnO NPs at the 300 K.

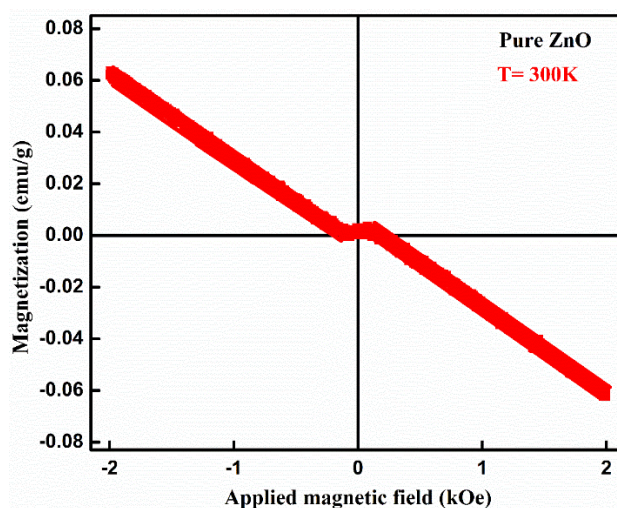The purely diamagnetic behavior of the ZnO at the low applied magnetic field supports the presence of oxygen vacancies (V_O) and zinc vacancies (V_{zn}), as described by PL spectrum [151]. Besides, the lattice distortion and the size effect can also be responsible for the diamagnetic magnetic behavior of the NPs [78].

5.3.7. Photocatalytic activity:

The photocatalytic activity (PCA) of ZnO had been tested for the photodegradation of an anionic congo red (CR) azo dye under UV irradiation. For the study, the dye concentration was chosen to be 5.0×10^{-5} M. Fig. 5.8 (a) shows the absorption of the CR dye in water. The maximum absorption corresponding to the lowest energy band is at 498 nm. The blank CR dye solution (without a mixture of ZnO catalyst) was kept under UV irradiation to examine the photolytic reaction. Still, there was no effect, hence no decomposition of dye without catalysts. Then, the typical dye degradation was performed in the presence of ZnO NPs as a catalyst (0.8 gL^{-1}) in an aqueous medium.

In this process, initially, the catalyst (ZnO NPs) was added to the dye solution and stirred in the dark for 1 h to reach the adsorption-desorption isotherm. Then 4 ml of the mixed solution was extracted from the sample and centrifuged at 7000 rpm for 2 min. The sample's absorption spectra were recorded before and after the exposure with UV illumination at specific intervals.

Before photoirradiation, the CR dye was degraded slowly, and the rate became extremely slow

after some intervals, i.e., the change in absorption is nearly minimal (Fig. 5.8a).
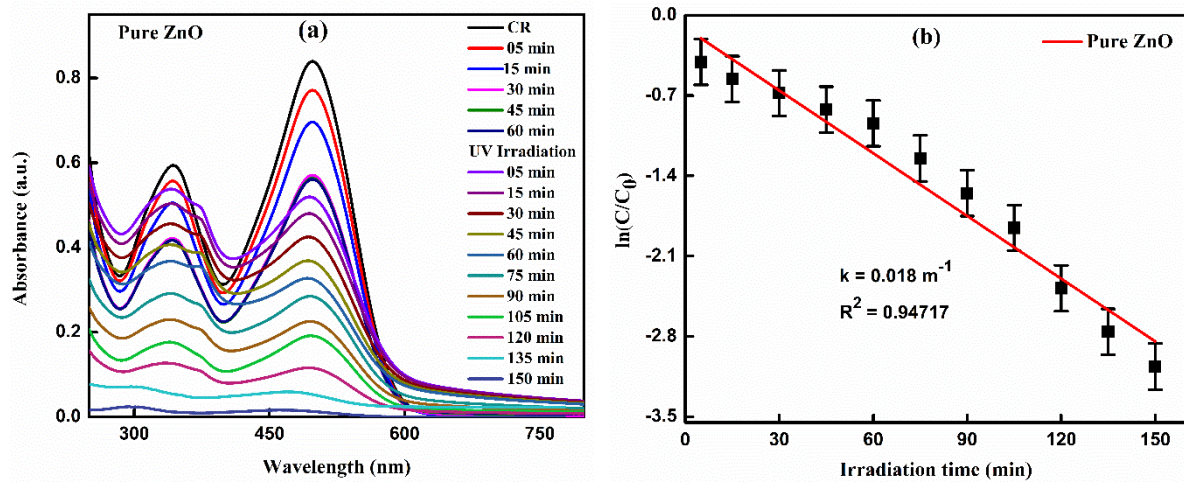
Fig. 5.8. The absorption spectra of CR dye in water in the presence of pure ZnO under UV

irradiation at different time intervals (a) and plot of ln(C/C$_0$) vs. *t* (irradiation time) (b).

After that, the specimen was kept under a UV lamp of 8 Watts, $\lambda \sim 254$ nm, and 1.2 mW/cm^2.

Upon the photoirradiation, the absorption intensity of CR dye decreases; hence the

photodegradation of dye started. Upon increasing the photoirradiation time, the absorption

intensity gradually decreased and became minimal at an irradiation time of 150 min. The

reaction rate constant of dye degradation has been calculated using pseudo-first-order kinetic

relation *ln (C/C$_0$) = -kt* [152]. Where 'C$_0$' and 'C' are the dye's absorbances at initial and after

a specific irradiation time, respectively. The '*k*' is the pseudo-first-order rate constant (min^{-1}),

and 't' is the photo-irradiation time (min). The reaction rate constant response is 0.018 min^{-1}

obtained from the linear fitted curve. The linear fitted curve is plotted between the *ln(C/C$_0$)* vs.

t (irradiation time) as shown in Fig 5.8(b). The degradation efficiency (DE) was estimated by

using Eq. 5.14 [153,154].

$$\text{Degradation efficiency (DE)\%} = \frac{C_0 - C}{C_0} \times 100 \qquad (5.14)$$

Where 'C' and 'C$_0$' are dye absorbances after irradiation and initial values, respectively. The

photodegradation efficiency of pure ZnO was calculated to be 98 %.

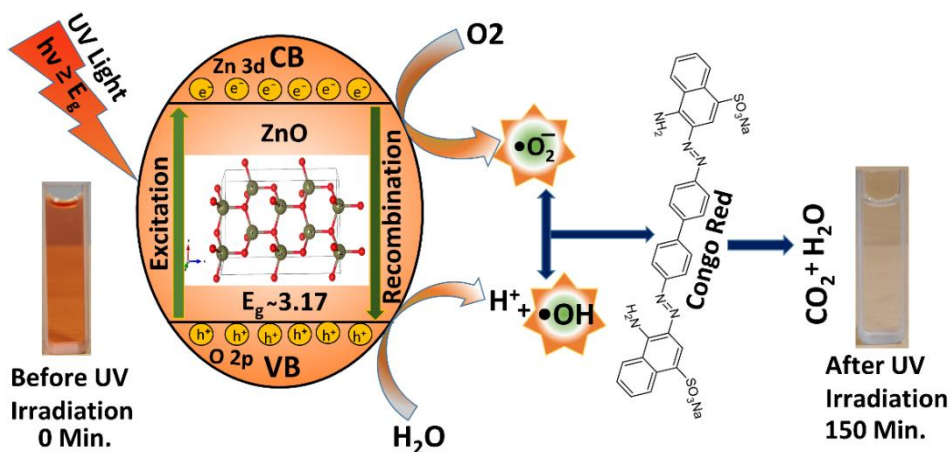**Fig. 5.9.** Schematic representation of the photocatalytic process and dye degradation in the presence of ZnO nanoparticles.

In the process of PCA, the electron-hole pairs are generated by the exposure of adequate UV light energy (hv) on the ZnO nanoparticles. The generated holes and electrons participate in the decomposition of CR dye, as demonstrated in Fig. 5.9.

$$ZnO + hv \text{ (UV irradiation)} \rightarrow ZnO \ (e^- \text{ - } h^+) \tag{5.15}$$
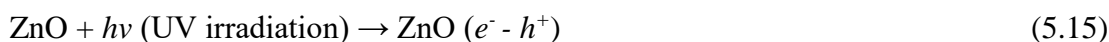
To produce hydroxyl (·OH), the holes (h^+) are formed when the valence band electrons of the catalyst react with electron donors, i.e., H_2O and hydroxyl ions (OH⁻) [155]. In the conduction band, the electrons react with the O_2 (oxygen molecule) on the ZnO surface to produce reactive super radical anions ($·O_2^-$) [156]. In the formation of hydroperoxyl radical (HO₂·), hydrogen peroxide (H_2O_2), the reaction will continue, and finally, the hydroxyl radicals are formed. Thus, the hole (h^+) and hydroperoxyl radicals are highly reactive intermediates attacking dye repeatedly and eventually decomposing dye or organic pollutants [157,158].

$$\text{Dye} + (HO_2·), \ (·O_2^-), \ (OH·) \rightarrow \text{intermediates} \rightarrow \text{final products} \tag{5.16}$$
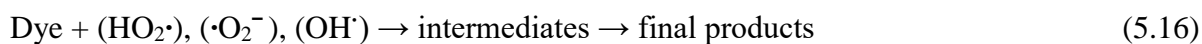
Nevertheless, trapping e^- in the CB to be scavenged through the e^- acceptors suppresses its recombination with the trapped hole.

5.4. Conclusions:

The pure ZnO NPs were produced via the facile sol-gel method. The structural and elemental investigations of the NPs were carried out with XRD, FESEM with EDAX, UV-vis, PL and

VSM. The observed crystallite size of the synthesized NP was ~20 nm. FESEM and EDAX images depict that the particles are in granular, spherical, and rod-like mixed-phase, and Zn, O elements exist in the ZnO NPs. The bandgap of NPs is ~3.17 eV obtained from the absorption spectrum. The PL spectrum demonstrates that the defects are present in the ZnO, which may be oxygen or zinc vacancy due to which diamagnetic behavior appears in the ZnO NPs. The CR dye degraded under UV irradiation. Within 150 min, the specific amount of dye is degraded entirely with 98% efficiency. Further studies of ZnO NPs with doping is under progress.

References

[1]   Z. Huang, H. Chen, Z.K. Chen, M.C. Roco, *J. Nanoparticle Res. 6 (2004) 325–354.*

[2]   S.K. Tripathi, R. Kaur, M. Rani, *Solid State Phenom. 222 (2015) 67–97.*

[3]   S.K. Tripathi, M. Rani, N. Singh, *Electrochim. Acta. 167 (2015) 179–186.*

[4]   E. Roduner, *Chem. Soc. Rev. 35 (2006) 583–592.*

[5]   R. Kaur, S.K. Tripathi, *Microelectron. Eng. 133 (2015) 59–65.*

[6]   *Food Chem. (2008) 8–92.*

[7]   N. Saifuddin, A.Z. Raziah, A.R. Junizah, *J. Chem. (2013).*

[8]   S. Lu, M. Li, D. Liu, Y. Yang, P. Yang, *J. Nanosci. Nanotechnol. 18 (2018) 288–295.*

[9]   Y. Yu, F. Cui, J. Sun, P. Yang, *Nano Lett. 16 (2016) 3078–3084.*

[10]   C.X. Shan, Z. Liu, S.K. Hark, *Appl. Phys. Lett. 90 (2007) 193123.*

[11]   C.G. Granqvist, *Thin Solid Films. 564 (2014) 1–38.*

[12]   S.V. Prylutska, I.I. Grynyuk, S.M. Grebinyk, O.P. Matyshevska, Y.I. Prylutskyy, U. Ritter, C. Siegmund, P. Scharff, *Materwiss. Werksttech. 40 (2009) 238–241.*

[13]   E.L. Dreizin, *Prog. Energy Combust. Sci. 35 (2009) 141–167.*

[14]   A. W. Bosman, and H. M. Janssen, E.W. Meijer*, *Chem. Rev. 99 (1999) 1665–1688.*

[15]   E.T. Thostenson, C. Li, T.W. Chou, *Compos. Sci. Technol. 65 (2005) 491–516.*

[16]   J. Geurts, *Springer Ser. Mater. Sci. 120 (2010) 7–37.*

[17]   C.W. Litton, D.C. Reynolds, T.C. Collins, *Zinc Oxide Mater. Electron. Optoelectron. Device Appl. (2011) 1–363.*

[18]   T.C. Damen, S.P.S. Porto, B. Tell, *Phys. Rev. 142 (1966) 570–574.*

[19]   C.W. Bunn, *Proc. Phys. Soc. 47 (1935) 835.*

[20]   G. Heiland, E. Mollwo, F. Stöckmann, *Solid State Phys. - Adv. Res. Appl. 8 (1959)*

191–323.

[21] S.P. Chang, R.W. Chuang, S.J. Chang, Y.Z. Chiou, C.Y. Lu, *Thin Solid Films. 517* (*2009*) *5054–5056.*

[22] Z.K. Tang, G.K.L. Wong, P. Yu, M. Kawasaki, A. Ohtomo, H. Koinuma, Y. Segawa, *Appl. Phys. Lett. 72* (*1998*) *3270.*

[23] D.C. Look, B. Claflin, *Phys. Status Solidi. 241* (*2004*) *624–630.*

[24] Z.L. Wang, *J. Phys. Condens. Matter. 16* (*2004*) *R829.*

[25] P. Pascariu, M. Homocianu, C. Cojocaru, P. Samoila, A. Airinei, M. Suchea, *Appl. Surf. Sci. 476* (*2019*) *16–27.*

[26] H. Karzel, W. Potzel, M. Köfferlein, W. Schiessl, M. Steiner, U. Hiller, G.M. Kalvius, D.W. Mitchell, T.P. Das, P. Blaha, K. Schwarz, M.P. Pasternak, *Phys. Rev. B. 53* (*1996*) *11425.*

[27] M.J.S. Spencer, *Prog. Mater. Sci. 3* (*2012*) *437–486.*

[28] H. C, T. A, H. C, P. A, Z. J, W. DG, *Nanoscale Res. Lett. 4* (*2009*) *1409–1420.*

[29] T. Xu, P. Ji, M. He, J. Li, *J. Nanomater. 2012* (*2012*).

[30] D.R. Lide, (*1991*).

[31] C. Wöll, Christof, *PrSS. 82* (*2007*) *55–120.*

[32] Z.L. Wang, *Mater. Today. 7* (*2004*) *26–33.*

[33] Y.R. Uhm, B.S. Han, M.K. Lee, S.J. Hong, C.K. Rhee, *Mater. Sci. Eng. A. 449–451* (*2007*) *813–816.*

[34] R. KM, F. K, B. J, W. DG, H. C, P. A, *Appl. Phys. Lett. 90* (*2007*).

[35] K. YY, C. YC, C. TJ, C. YM, L. PS, *Toxicol. Sci. 125* (*2012*) *462–472.*

[36] C. Klingshirn, *ChemPhysChem. 8* (*2007*) *782–803.*

[37] Y. Zhang, M.K. Ram, E.K. Stefanakos, D.Y. Goswami, *J. Nanomater. 2012* (*2012*).

[38] Y. Tokura, M. Kawasaki, N. Nagaosa, *Nat. Phys. 2017 1311. 13* (*2017*) *1056–1068.*

[39] A. Sundaresan, R. Bhargavi, N. Rangarajan, U. Siddesh, C.N.R. Rao, *Phys. Rev. B. 74* (*2006*) *161306.*

[40] B. Panigrahy, M. Aslam, D.S. Misra, M. Ghosh, D. Bahadur, *Adv. Funct. Mater. 20* (*2010*) *1161–1165.*

[41] G.H. Mhlongo, D.E. Motaung, S.S. Nkosi, H.C. Swart, G.F. Malgas, K.T. Hillie, B.W. Mwakikunga, *Appl. Surf. Sci. 293* (*2014*) *62–70.*

[42] C. V. Manzano, D. Alegre, O. Caballero-Calero, B. Alén, M.S. Martín-González, *J. Appl. Phys. 110* (*2011*) *043538.*

[43] S.A. Chambers, T.C. Droubay, C.M. Wang, K.M. Rosso, S.M. Heald, D.A. Schwartz, K.R. Kittilstved, D.R. Gamelin, *Mater. Today. 9* (*2006*) *28–35.*

[44] T. Fukumura, Z. Jin, A. Ohtomo, H. Koinuma, M. Kawasaki, *Appl. Phys. Lett. 75*

(*1999*) *3366*.

[45] T. Dietl, H. Ohno, F. Matsukura, J. Cibert, D. Ferrand, *Science (80-.). 287 (2000) 1019–1022*.

[46] K. Rekha, M. Nirmala, M.G. Nair, A. Anukaliani, *Phys. B Condens. Matter. 405 (2010) 3180–3185*.

[47] O.D. Jayakumar, C. Sudakar, C. Persson, V. Sudarsan, R. Naik, A.K. Tyagi, *J. Phys. Chem. C. 114 (2010) 17428–17433*.

[48] L. Peng, J. Zhai, D. Wang, Y. Zhang, P. Wang, Q. Zhao, T. Xie, *Sensors Actuators B Chem. 148 (2010) 66–73*.

[49] X. Zhang, M. Wu, W. Diao, B. Zhang, J. Hao, Z. Xu, R. Chu, *Phys. B Condens. Matter. 474 (2015) 1–4*.

[50] N.H. Hong, J. Sakai, A. Hassini, *J. Appl. Phys. 97 (2005) 10D312*.

[51] S. Kuriakose, B. Satpati, S. Mohapatra, *Phys. Chem. Chem. Phys. 16 (2014) 12741–12749*.

[52] G. Poongodi, P. Anandan, R.M. Kumar, R. Jayavel, *Spectrochim. Acta - Part A Mol. Biomol. Spectrosc. 148 (2015) 237–243*.

[53] H. Gu, W. Zhang, Y. Xu, M. Yan, *Appl. Phys. Lett. 100 (2012) 202401*.

[54] G. Vijayaprasath, R. Murugan, S. Asaithambi, P. Sakthivel, T. Mahalingam, Y. Hayakawa, G. Ravi, *Ceram. Int. 42 (2016) 2836–2845*.

[55] L.T. Tseng, A. Suter, Y.R. Wang, F.X. Xiang, P. Bian, X. Ding, A. Tseng, H.L. Hu, H.M. Fan, R.K. Zheng, X.L. Wang, Z. Salman, T. Prokscha, K. Suzuki, R. Liu, S. Li, E. Morenzoni, J.B. Yi, *Phys. Rev. B. 96 (2017) 104423*.

[56] C.M. Chang, M.H. Hon, I.C. Leu, *Sensors Actuators B Chem. 151 (2010) 15–20*.

[57] S.K. Arora, A. Devi, V.S. Jaswal, J. Singh, M. Kinger, V.D. Gupta, *Orient. J. Chem. 30 (2014) 1671–1679*.

[58] B. Xiao, H. Liu, V. Avrutin, J.H. Leach, E. Rowe, H. Liu, Ü. Özgür, H. Morkoç, W. Chang, L.M.B. Alldredge, S.W. Kirchoefer, J.M. Pond, *Appl. Phys. Lett. 95 (2009) 212901*.

[59] H. Shokry Hassan, A.B. Kashyout, I. Morsi, A.A.A. Nasser, I. Ali, *Beni-Suef Univ. J. Basic Appl. Sci. 3 (2014) 216–221*.

[60] Y. Gong, T. Andelman, G.F. Neumark, S. O'Brien, I.L. Kuskovsky, *Nanoscale Res. Lett. 2007 26. 2 (2007) 297–302*.

[61] M.F. Khan, A.H. Ansari, M. Hameedullah, E. Ahmad, F.M. Husain, Q. Zia, U. Baig, M.R. Zaheer, M.M. Alam, A.M. Khan, Z.A. AlOthman, I. Ahmad, G.M. Ashraf, G. Aliev, *Sci. Reports 2016 61. 6 (2016) 1–12*.

[62] R. Podila, B. Anand, J.P. West, R. Philip, S.S.S. Sai, J. He, M. Skove, S.-J. Hwu, S. Tewari, A.M. Rao, *Nanotechnology. 22 (2011) 095703*.

[63] C. Xiao, J. Yan, T. Li, *J. Nanomater. 2014 (2014)*.

[64]   Y. Zhang, J. Xu, Q. Xiang, H. Li, Q. Pan, P. Xu, (n.d.).

[65]   J. N, R. B, R. KT, M. AC, *FEMS Microbiol. Lett. 279* (*2008*) *71–76*.

[66]   O. Harnack, C. Pacholski, H. Weller, A. Yasuda, J.M. Wessels, *Nano Lett. 3* (*2003*) *1097–1101*.

[67]   Arie Wibowo, M. Agung Marsudi, M. Ikhlasul Amal, M. Bagas Ananda, Ruth Stephanie, Husaini Ardy, L. Jaya Diguna, *RSC Adv. 10* (*2020*) *42838–42859*.

[68]   S.-J. Young, Y.-H. Liu, J.-T. Chien, *ACS Omega. 3* (*2018*) *8135*.

[69]   M.F.M. Fathil, M.K.M. Arshad, U. Hashim, A.R. Ruslinda, R.M. Ayub, S.C.B. Gopinath, C.H. Voon, K.L. Foo, R. Adzhri, M.N.M. Nuzaihan, A.H. Azman, M. Zaki, *RSM 2015 - 2015 IEEE Reg. Symp. Micro Nano Electron. Proc.* (*2015*).

[70]   J.M. Coronado, *Green Energy Technol. 71* (*2013*) *1–4*.

[71]   E. Baur, C. Neuweiler, *Helv. Chim. Acta. 10* (*1927*) *901–907*.

[72]   G. Oster, *J. Phys. Chem. 70* (*1966*) *3033–3036*.

[73]   Y.C. Kang, S. Bin Park, I.W. Lenggoro, K. Okuyama, *J. Mater. Res. 14* (*1999*) *2611–2615*.

[74]   L. Jing, F. Yuan, H. Hou, B. Xin, W. Cai, H. Fu, *Sci. China Ser. B Chem. 2005 481. 48* (*2005*) *25–30*.

[75]   Y.J. Li, C.Y. Wang, M.Y. Lu, K.M. Li, L.J. Chen, *Cryst. Growth Des. 8* (*2008*) *2598–2602*.

[76]   J. Wang, Z. Wang, B. Huang, Y. Ma, Y. Liu, X. Qin, X. Zhang, Y. Dai, (*2012*).

[77]   S. Balachandran, S.G. Praveen, R. Velmurugan, M. Swaminathan, *RSC Adv. 4* (*2014*) *4353–4362*.

[78]   A. Chanda, S. Gupta, M. Vasundhara, S.R. Joshi, G.R. Mutta, J. Singh, *RSC Adv. 7* (*2017*) *50527–50536*.

[79]   A. Chanda, S. Gupta, M. Vasundhara, S.R. Joshi, G.R. Mutta, J. Singh, *RSC Adv. 7* (*2017*) *50527–50536*.

[80]   N.K. Singh, V. Koutu, M.M. Malik, *J. Sol-Gel Sci. Technol. 91* (*2019*) *324–334*.

[81]   E. Bellingeri, S. Rusponi, A. Lehnert, H. Brune, F. Nolting, A. Leveratto, A. Plaza, D. Marré, *Sci. Reports 2019 91. 9* (*2019*) *1–12*.

[82]   P.R. Chithira, T. Theresa John, *J. Magn. Magn. Mater. 496* (*2020*) *165928*.

[83]   M.K. Singh, M.S. Mehata, *Optik (Stuttg). 193* (*2019*) *163011*.

[84]   D. Chateigner, *J. Appl. Crystallogr. 41* (*2008*) *826–827*.

[85]   H.-H. Perkampus, *UV-VIS Spectrosc. Its Appl.* (*1992*) *1–2*.

[86]   V. Sharma, M.S. Mehata, *Mater. Res. Bull. 134* (*2021*) *111121*.

[87]   H.-H. Perkampus, *UV-VIS Spectrosc. Its Appl.* (*1992*) *3–9*.

[88]   H.-H. Perkampus, *UV-VIS Spectrosc. Its Appl.* (*1992*) *10–25*.

[89]   J.R. Lakowicz, *Princ. Fluoresc. Spectrosc.* (*1983*) *1–18*.

[90]   P. Sharma, M.S. Mehata, *Mater. Res. Bull. 131* (*2020*) *110978*.

[91]   J.R. Lakowicz, *Princ. Fluoresc. Spectrosc.* (*1983*) *19–49*.

[92]   R. Singh, *Phys. Perspect. 4* (*2002*) *399–420*.

[93]   C.L. Du, Z.B. Gu, M.H. Lu, J. Wang, S.T. Zhang, J. Zhao, G.X. Cheng, H. Heng, Y.F. Chen, *J. Appl. Phys. 99* (*2006*).

[94]   J.I. Goldstein, D.E. Newbury, P. Echlin, D.C. Joy, C.E. Lyman, E. Lifshin, L. Sawyer, J.R. Michael, *Scanning Electron Microsc. X-Ray Microanal.* (*2003*) *1–20*.

[95]   J.I. Goldstein, D.E. Newbury, P. Echlin, D.C. Joy, C.E. Lyman, E. Lifshin, L. Sawyer, J.R. Michael, *Scanning Electron Microsc. X-Ray Microanal.* (*2003*) *21–60*.

[96]   J.I. Goldstein, D.E. Newbury, P. Echlin, D.C. Joy, C.E. Lyman, E. Lifshin, L. Sawyer, J.R. Michael, *Scanning Electron Microsc. X-Ray Microanal.* (*2003*) *297–353*.

[97]   W. Becker, *J. Microsc. 247* (*2012*) *119–136*.

[98]   Y. Kumar, A. Sahai, S.F. Olive-Méndez, N. Goswami, V. Agarwal, *Ceram. Int. 42* (*2016*) *5184–5194*.

[99]   T.M. Hammad, J.K. Salem, R.G. Harrison, *Appl. Nanosci. 3* (*2013*) *133–139*.

[100]   S. Talam, S.R. Karumuri, N. Gunnam, *ISRN Nanotechnol. 2012* (*2012*) *1–6*.

[101]   I.A. Kariper, *Opt. Mater. (Amst). 44* (*2015*) *78–83*.

[102]   J. Singh, A. Chanda, S. Gupta, P. Shukla, V. Chandra, *AIP Conf. Proc. 1731* (*2016*) *1–4*.

[103]   S.U. Awan, Z. Mehmood, S. Hussain, S.A. Shah, N. Ahmad, M. Rafique, M. Aftab, T.A. Abbas, *Phys. E Low-Dimensional Syst. Nanostructures. 103* (*2018*) *110–121*.

[104]   S.S. Ghosh, C. Choubey, A. Sil, *Superlattices Microstruct. 125* (*2019*) *271–280*.

[105]   A. Mesaros, C.D. Ghitulica, M. Popa, R. Mereu, A. Popa, T. Petrisor, M. Gabor, A.I. Cadis, B.S. Vasile, *Ceram. Int. 40* (*2014*) *2835–2846*.

[106]   R. Alsharafi, Y. Zhu, F. Li, Z. Xu, H. Hu, T. Guo, *Org. Electron. 75* (*2019*).

[107]   M.K. Lima, D.M. Fernandes, M.F. Silva, M.L. Baesso, A.M. Neto, G.R. de Morais, C.V. Nakamura, A. de Oliveira Caleare, A.A.W. Hechenleitner, E.A.G. Pineda, *J. Sol-Gel Sci. Technol. 72* (*2014*) *301–309*.

[108]   P.G. Devi, A.S. Velu, *J. Theor. Appl. Phys. 10* (*2016*) *233–240*.

[109]   H. Sutanto, S. Wibowo, Hadiyanto, M. Arifin, E. Hidayanto, *Mater. Res. Express. 4* (*2017*).

[110]   A. Guler, L. Arda, N. Dogan, C. Boyraz, E. Ozugurlu, *Ceram. Int. 45* (*2019*) *1737–1745*.

[111]   M.J. Chithra, K. Pushpanathan, M. Loganathan, *Mater. Manuf. Process. 29* (*2014*) *771–779*.

[112] P. Swapna, S. Venkatramana Reddy, *IOP Conf. Ser. Mater. Sci. Eng. 310* (*2018*).

[113] Y. Tu, Q. Fu, X. Niu, J. Sang, Z. Tan, X. Zou, *J. Mater. Sci. Technol. 29* (*2013*) *1053–1058.*

[114] N. Güy, S. Çakar, M. Özacar, *J. Colloid Interface Sci. 466* (*2016*) *128–137.*

[115] N. Jamal, A. Radhakrishnan, R. Raghavan, B. Bhaskaran, *Main Gr. Met. Chem. 43* (*2020*) *84–91.*

[116] Y.-T. Huang, M.-C. Shih, *Int. J. Sci. Res. Publ. 6* (*2016*) *549.* www.ijsrp.org.

[117] M.S. Mehata, R.K. Ratnesh, *Dalt. Trans. 48* (*2019*) *7619–7631.*

[118] H. Ji, C. Cai, S. Zhou, W. Liu, *J. Mater. Sci. Mater. Electron. 29* (*2018*) *12917–12926.*

[119] M.G. Nair, M. Nirmala, K. Rekha, A. Anukaliani, *Mater. Lett. 65* (*2011*) *1797–1800.*

[120] M.I. Khan, M. Naeem, G.M. Mustafa, S.A. Abubshait, A. Mahmood, W. Al-Masry, N.Y.A. Al-Garadi, S.M. Ramay, *Ceram. Int. 46* (*2020*) *26590–26597.*

[121] F. Hassan, M. Miran, H. Simol, M.H. Susan, M. Mollah, *Bangladesh J. Sci. Ind. Res. 50* (*2015*) *21–28.*

[122] Islah-u-din, W.T. Salam, S.S.A. Gillani, M.B. Tahir, M. Ikram, S. Ali, *Optik (Stuttg). 203* (*2020*) *163966.*

[123] R. He, B. Tang, C. Ton-That, M. Phillips, T. Tsuzuki, *J. Nanoparticle Res. 15* (*2013*).

[124] G. Vijayaprasath, R. Murugan, S. Asaithambi, P. Sakthivel, T. Mahalingam, Y. Hayakawa, G. Ravi, *Ceram. Int. 42* (*2016*) *2836–2845.*

[125] G. Gupta, S. Verma, R. Nagarajan, S. Rath, *Phys. B Condens. Matter. 604* (*2021*) *412735.*

[126] T. Srinivasulu, K. Saritha, K.T.R. Reddy, *Mod. Electron. Mater. 3* (*2017*) *76–85.*

[127] A. Khorsand Zak, W.H. Abd. Majid, M.E. Abrishami, R. Yousefi, *Solid State Sci. 13* (*2011*) *251–256.*

[128] A. Tiwari, P.P. Sahay, *Opt. Mater. (Amst). 110* (*2020*) *110395.*

[129] A.K. Rana, Y. Kumar, P. Rajput, S.N. Jha, D. Bhattacharyya, P.M. Shirage, *ACS Appl. Mater. Interfaces. 9* (*2017*) *7691–7700.*

[130] C. Thirupathi, S. Nithiyanantham, M. Sentilkumar, A. Arivudainambi, S. Mahalakshmi, B. Natarajan, *Adv. Sci. Eng. Med. 12* (*2020*) *524–529.*

[131] D. Zhang, D. Wu, Y. Cao, X. Zong, Z. Yang, *J. Mater. Sci. Mater. Electron. 29* (*2018*) *19558–19566.*

[132] F.Meydaner. Tezel, I.Af. Kariper, *Surf. Rev. Lett. 27* (*2020*) *1–7.*

[133] T. Wang, Y. Liu, Q. Fang, M. Wu, X. Sun, F. Lu, *Appl. Surf. Sci. 257* (*2011*) *2341–2345.*

[134] D. Anbuselvan, S. Muthukumaran, M. Ashokkumar, *J. Mater. Sci. Mater. Electron. 25* (*2014*) *2004–2015.*

[135] M. Fang, C.M. Tang, Z.W. Liu, *J. Electron. Mater. 47* (*2018*) *1390–1396*.

[136] S.K. Tripathy, *Opt. Mater. (Amst). 46* (*2015*) *240–246*.

[137] N.M. Ravindra, P. Ganapathy, J. Choi, *Infrared Phys. Technol. 50* (*2007*) *21–29*.

[138] T.S. Moss, *Phys. Status Solidi. 131* (*1985*) *415–427*.

[139] V.P. Gupta, N.M. Ravindra, *Phys. Status Solidi. 100* (*1980*) *715–719*.

[140] S. Notes, V.K. Srivastava, *55* (*1979*).

[141] P. Hervé, L.K.J. Vandamme, *Infrared Phys. Technol. 35* (*1994*) *609–615*.

[142] R.R. Reddy, S. Anjaneyulu, *Phys. Status Solidi. 174* (*1992*) *K91–K93*.

[143] R.R. Reddy, Y. Nazeer Ahammed, *Infrared Phys. Technol. 36* (*1995*) *825–830*.

[144] V. Kumar, J.K. Singh, *Indian J. Pure Appl. Phys. 48* (*2010*) *571–574*.

[145] A. Kaphle, P. Hari, *J. Appl. Phys. 122* (*2017*).

[146] S.D. Senol, E. Ozugurlu, L. Arda, *J. Alloys Compd. 822* (*2020*) *153514*.

[147] B. Salameh, A.M. Alsmadi, M. Shatnawi, *J. Alloys Compd. 835* (*2020*) *155287*.

[148] N. Srinatha, P. Raghu, H.M. Mahesh, B. Angadi, *J. Alloys Compd. 722* (*2017*) *888–895*.

[149] R. Bhardwaj, K.H. Chae, N. Goyal, *Vacuum. 178* (*2020*) *109446*.

[150] D. Behera, B.S. Acharya, *J. Lumin. 128* (*2008*) *1577–1586*.

[151] M.P. Dasari, U. Godavarti, V. Mote, *Process. Appl. Ceram. 12* (*2018*) *100–110*.

[152] M.K. Singh, M.S. Mehata, *Opt. Mater. (Amst). 109* (*2020*).

[153] P. Debnath, N.K. Mondal, *Environ. Nanotechnology, Monit. Manag. 14* (*2020*) *100320*.

[154] S. Chakraborty, J.J. Farida, R. Simon, S. Kasthuri, N.L. Mary, *Surfaces and Interfaces. 19* (*2020*) *100488*.

[155] S.M. Lam, J.C. Sin, A.Z. Abdullah, A.R. Mohamed, *Desalin. Water Treat. 41* (*2012*) *131–169*.

[156] A. Sadollahkhani, Z. Hussain Ibupoto, S. Elhag, O. Nur, M. Willander, *Ceram. Int. 40* (*2014*) *11311–11317*.

[157] A. Sadollahkhani, I. Kazeminezhad, J. Lu, O. Nur, L. Hultman, M. Willander, *RSC Adv. 4* (*2014*) *36940–36950*.

[158] R.E. Adam, G. Pozina, M. Willander, O. Nur, *Photonics Nanostructures - Fundam. Appl. 32* (*2018*) *11–18*.

Fwd: [IJEMS] Editor Decision (IJEMS-2896)

1 message

Mohan Mehata <msmehata@gmail.com>   Fri, Jul 30, 2021 at 11:13 AM
To: m180035@nitsikkim.ac.in

---------- Forwarded message ---------
From: **Ms. Meetali Bharti** <op.niscair@gmail.com>
Date: Fri, Jul 30, 2021 at 11:08 AM
Subject: [IJEMS] Editor Decision (IJEMS-2896)
To: Mr. Mohan Singh Mehata <msmehata@gmail.com>

Dear Mr. Mohan Singh Mehata,

We have reached a decision regarding your submission to Indian Journal of
Engineering and Materials Sciences (IJEMS), "Synthesis and characterization
of diamagnetic ZnO Nano-Crystallites derived via sol-gel method for
photocatalytic activity (Article Id: IJEMS-2896)".

Our decision is to: Accept Submission

This is an automatically generated email. Please, don't reply to this email.

Ms. Meetali Bharti
Scientist, CSIR-NISCAIR, New Delhi, India
ijems@niscair.res.in

Editor
Indian Journal of Engineering and Materials Sciences (IJEMS)
http://op.niscair.res.in/index.php/IJEMS

--

Dr. Mohan Singh Mehata
(Former JSPS and CAS Fellow)
Assistant Professor
Laser-Spectroscopy Laboratory
Department of Applied Physics
Delhi Technological University
(Formerly Delhi College of Engineering)
Bawana Road, Delhi 110042.
Mob. +91-9953142553
E-mail: msmehata@gmail.com; msmehata@dtu.ac.in
https://www.sites.google.com/site/mohansmehata/
https://www.researchgate.net/profile/Mohan_Mehata